NASA Technical Paper 1402
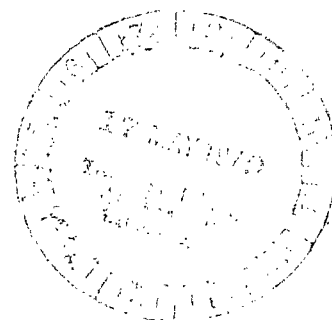
Analyses of Earth Radiation Budget Data From Unrestricted Broadband Radiometers on the ESSA 7 Satellite

William L. Weaver and Frederick B. House

MAY 1979

NASA

NASA Technical Paper 1402

Analyses of Earth Radiation Budget Data From Unrestricted Broadband Radiometers on the ESSA 7 Satellite

William L. Weaver
Langley Research Center
Hampton, Virginia

and

Frederick B. House
Drexel University
Philadelphia, Pennsylvania

SUMMARY

Six months of data (Sept. 1968 through Feb. 1969) from the wide-field-of-view low resolution infrared radiometers (LRIR) on the Environmental Science Services Administration (ESSA) 7 satellite were analyzed. Earth-emitted and Earth-reflected irradiances were computed at satellite altitude using data from a new in-flight calibration technique. Flux densities and albedos were computed for the top of the Earth's atmosphere (30 km). Monthly averages of these quantities over 10°-latitude zones, each hemisphere, and the globe are presented for each month analyzed, and global distributions are presented for typical months. Emitted flux densities are generally lower and albedos higher than those of previous studies. This may be due, in part, to the fact that the ESSA 7 satellite was in a 3-p.m. Sun-synchronous orbit and some of the comparison data were obtained from satellites in 12-noon Sun-synchronous orbits. ESSA 7 detectors seem to smooth out spatial flux density variations more than scanning radiometers or wide-field-of-view fixed-plate detectors. Significant longitudinal and latitudinal variations of emitted flux density and albedo were identified in the tropics in a zone extending about ±25° in latitude.

INTRODUCTION

Solar energy plays the dominant role in generating the Earth's weather and climate. Our capability to study this role took a giant step forward with the advent of artificial Earth satellites, since they provide excellent platforms from which to monitor the amounts of solar energy which the Earth reflects, absorbs, and reemits. Starting with Explorer 7 in 1960, instruments for measuring components of the Earth's radiation budget have been flown on about half the United States meteorological satellites. Earth radiation budget results from the first generation of these meteorological satellites (1960 through 1965) were reported in reference 1.

Included in the second generation of meteorological satellites, which began in 1966, was the ESSA series. Radiation measurements made with the low resolution infrared radiometers (LRIR) on the ESSA satellites are an important subset of the radiation measurements of the late 1960's. Descriptions of techniques for analyzing these data and results from very limited analyses of the radiation data from ESSA 3 are given in references 2 and 3, but no previous paper has directly reported results from radiation analyses of the ESSA 7 satellite data. One possible reason that the ESSA data have been largely ignored was a detector degradation problem which was caused by continued exposure to solar radiation. In references 2 and 3, techniques are described for overcoming this problem using in-flight data, and an improved technique for flight calibrating the detectors was reported in reference 4. The new technique requires neither the assumptions concerning the behavior of emitted flux density at spacecraft ingression and egression that are required by the techniques of references 2 and 3 nor the assumptions relative to net flux density required in reference 3.

This paper describes results of an analysis of ESSA 7 radiation data using the in-flight calibration technique of reference 4. Irradiances are computed at the satellite, and flux densities and albedos are determined for the top of the Earth's atmosphere. Flux densities and albedos are presented for each month of data analyzed, and global distributions of these parameters are shown for typical months. ESSA 7 results are discussed relative to results from several previous radiation budget analyses, and some results are compared directly to other results.

SYMBOLS

A	albedo, ratio of reflected to incident solar flux density
a_i	area of ith 10°-latitude zone, m^2
C	detector housing constant
E	irradiance, W/m^2
F	geometric shape factor
H_s	solar flux density at mean distance from Earth to Sun, W/m^2
h	measurement (satellite) altitude, km
h_0	reference altitude (top of atmosphere), 30 km
K'	thermal mass coefficient of detector, $J/m^2 \cdot K$
L	distance from Earth to Sun, normalized by mean distance
M	radiant flux density or exitance, W/m^2
R	radius of Earth, 6371 km
T	temperature, K
α	absorptance of detector
(α/ϵ)	detector response factor
β	spherical coordinate defined in figure 18
γ	angle between spacecraft spin axis and Sun, deg
ϵ	emittance of detector
η	spherical coordinate defined in figure 18

η_{max} unrestricted view angle of Earth horizon from detector

θ latitude

λ longitude

ξ angle incoming ray makes with normal to detector surface

σ Stefan-Boltzmann constant, 5.66961×10^{-8} W/m$^2 \cdot$K^4

ϕ Sun zenith angle at subsatellite point, deg

$d\omega$ solid angle at detector subtended by increment of area

Subscripts:

A   ascent

av   average

b   black-coated

D   descent

d   detector

e   Earth emitted, longwave

G   globe or entire Earth surface

h   detector housing

n   net

r   Earth reflected, shortwave

s   direct solar

w   white-coated

Other notations:

$\cos^* \phi$ function (defined in fig. 5) for computing albedo

Bar over quantity denotes monthly average.

Dot over quantity denotes derivation with respect to time.

3

SATELLITE ORBIT AND DATA SET CHARACTERISTICS

Orbit

The ESSA 7 meteorological satellite was launched by NASA on August 16, 1968. The orbit was Sun synchronous and nearly circular with an average altitude of 1450 km, a period of 114.7 min, and an inclination of 102°. The satellite crossed the equator during ascent (going northward) at a mean local time of 3 p.m. The average local time is shown in figure 1 as a function of satellite latitude. Measurements were made every 30 sec, or about every 1.6° of Earth central angle. At an altitude of 1450 km, the spacecraft is in direct sunlight at subsatellite-point Sun zenith angles up to about 123°, whereas the terminator at the Earth's surface occurs at a Sun zenith angle of 90°. Ingression and egression as used herein will refer to the spacecraft's entry into and exit from direct sunlight. This always occurs on the descent portion of the orbit so that during ascent the spacecraft is continuously exposed to direct solar radiation.

Data Collection

Measurements were made almost continuously from August 16, 1968, to July 19, 1969. The data set obtained from the Environmental Data Service of the National Oceanic and Atmospheric Administration (NOAA) covered the period from Sept. 1, 1968, to May 31, 1969. Data for the second two weeks of December were missing from this set, and sampling for the first two weeks of December was not as complete as for the other months. Due to anomalies in the data of March, April, and May, 1969, results reported herein are for the period September 1968 through February 1969 only.

Because the orbit is Sun synchronous, the local, or Sun time, at which the spacecraft crosses a given latitude, on ascent or descent, is essentially constant. This means that the average emitted flux density at a given latitude is based on measurements made at only two local times (one on ascent, one on descent). Average reflected flux densities and albedo at the same latitudes are based on ascent measurements, only, and thus include measurements at only one local time. In references 1 and 5, variations in emitted flux densities with local time were found. A significant effect on albedo due to local time was also found in reference 1. Many of the other results discussed in this paper are based on data sets obtained with Sun-synchronous orbits. The data of reference 6 were obtained with a 3-p.m. orbit, those of reference 7 were obtained in a 12-noon orbit, and some of the data of references 1 and 8 were obtained with satellites having various Sun-synchronous orbits.

Data Editing

Four different data editing schemes were used to eliminate bad or uncertain data. The first scheme, described in reference 4, eliminated points when the measurements were obviously inconsistent with the orbit ephemeris or when there were inconsistencies in the ephemeris itself. For instance, measurements might indicate that the spacecraft was in direct sunlight while the ephemeris showed

the spacecraft was in darkness, or the spacecraft position would be inconsistent with the Sun zenith angle.

The second editing scheme dealt with data in the transition regions where rapid heating and cooling of the detectors at ingression and egression produced uncertainties in the measurements. Data in these regions were rejected when the Sun zenith angles were in the range from 123° to 127°. The zones affected were always on the descent portion of the orbit, and for the affected zones, the distributions may not be centered in the zone.

In the third editing scheme, data were eliminated when the computed emitted irradiance was found to lie outside a given envelope. For each latitude zone, an envelope was given which was based on a computed value of the estimated mean and variations about the mean. This scheme takes into account the significant pole-to-equator gradient in the mean emitted flux density as well as changes in the variation about the mean from zone to zone.

The fourth editing scheme eliminated data when the magnitude of the computed irradiance changed more than a specified amount in a specified time. This scheme can reject spurious data spikes where the magnitude of the irradiance could be within the envelope specified in the third editing scheme.

Spatial Sampling

Spatial sampling, both in number of measurements and in distribution, is believed to be adequate for each of the six-month periods analyzed. Contours showing the spatial distribution of the edited sample for October 1968 (which is typical) are presented in figure 2 for both the ascent and descent portions of the orbit. These contours are based on the number of samples in regions of 10° latitude by 10° longitude. The distribution is seen to be quite uniform during ascent. The less uniform distribution during descent is due mainly to the elimination of data at spacecraft ingression and egression.

DESCRIPTION OF DETECTORS AND MEASUREMENTS

ESSA 7 was a spin-stabilized satellite with its spin axis normal to the orbit plane. Each detector consisted of a pair of flat-plate, bolometer-type radiometers wired in electrical series and mounted opposite each other on the outer circumference of the spacecraft. The temperatures of the detectors T_d and of the housings which support the detectors T_h are the basic measured signals. A more complete discussion of the ESSA 7 detectors can be found in references 2 and 4. Each radiometer alternately views the Earth and space, and the integrated signal from the two radiometers is treated as an average measurement over the rotation period of about 6.5 sec. The instrument system was made up of two detectors. Each detector has different surface property (called white or black) to discriminate longwave- and shortwave-radiation components. Each detector is in radiation equilibrium. That is,

$$E_d = M_d \qquad (1)$$

where E_d, the irradiance absorbed by the detector from external sources, is given by:

$$E_d = (\alpha/\epsilon)_e E_e + (\alpha/\epsilon)_r E_r + (\alpha/\epsilon)_s E_s \tag{2}$$

and M_d, the exitance at the detector, is calculated, using the measured temperatures of the detector and its housing, by the equation

$$M_d = \sigma T_d^4 + \sigma C\left(T_d^4 - T_h^4\right) + K'\dot{T}_d \tag{3}$$

The equation for the irradiance absorbed by the detector (eq. (2)) can be simplified in two ways.

First, a detector's response to Earth-reflected radiation and to direct solar radiation will be the same since these two radiation sources have essentially the same spectral characteristics. That is,

$$(\alpha/\epsilon)_s \equiv (\alpha/\epsilon)_r$$

Second, we will assume that we can independently compute a value for the direct solar irradiance E_s. Now if we let $M_{d,w}$ be the calculated value of radiant exitance for the white-coated detector (eq. (3)) and if we make use of the equilibrium relationship (eq. (1)), we have

$$M_{d,w} = (\alpha/\epsilon)_{e,w}E_e + (\alpha/\epsilon)_{r,w}E_r + (\alpha/\epsilon)_{r,w}E_s \tag{4a}$$

Similarly for the black-coated detector, we have

$$M_{d,b} = (\alpha/\epsilon)_{e,b}E_e + (\alpha/\epsilon)_{r,b}E_r + (\alpha/\epsilon)_{r,b}E_s \tag{4b}$$

Equations (4a) and (4b) can be solved simultaneously for the Earth-emitted and Earth-reflected components of irradiance, E_e and E_r.

$$E_e = \frac{M_{d,b}(\alpha/\epsilon)_{r,w} - M_{d,w}(\alpha/\epsilon)_{r,b}}{(\alpha/\epsilon)_{r,w}(\alpha/\epsilon)_{e,b} - (\alpha/\epsilon)_{r,b}(\alpha/\epsilon)_{e,w}} \tag{5a}$$

6

$$E_r = \frac{M_{d,w}(\alpha/\varepsilon)_{e,b} - M_{d,b}(\alpha/\varepsilon)_{e,w}}{(\alpha/\varepsilon)_{r,w}(\alpha/\varepsilon)_{e,b} - (\alpha/\varepsilon)_{r,b}(\alpha/\varepsilon)_{e,w}} - E_s \qquad (5b)$$

The section which follows describes how the detector characteristics required to compute emitted and reflected irradiances at the satellite were determined by equations (5a) and (5b).

DETECTOR CHARACTERISTICS

Coefficients Required for Computations of Detector Exitance

Values for the detector housing constants C required to calculate the detector exitance by equation (3) were determined in preflight laboratory calibration tests. The calibration procedure, which consisted of testing a flight version of the detector, is described in reference 4. The resultant detector housing constants were found to be

$$C_w \ldots \ldots \ldots 0.075$$

$$C_b \ldots \ldots \ldots 0.054$$

The detector thermal mass coefficients K' were calculated using flight data obtained during spacecraft ingression and egression. The calculations are described in reference 4, and the resulting thermal mass coefficients are plotted in figure 3 as a function of detector temperature. Exitance due to changes in detector temperature (thermal mass term in eq. (3)) was small outside the regions of ingression and egression because temperature changes were gradual. Abrupt temperature changes inside these regions, however, resulted in sharp changes in exitance, and some measurements had to be rejected.

Detector Response to Longwave Radiation

Determination of absorptance and emittance of the two (black and white) detectors for emitted radiation was made for several temperatures and included spectral absorptance data for the two detector coatings. The spectral absorptance curves and the values of absorptance and emittance as functions of temperature are given in reference 4. One value of longwave absorptance was selected for each detector. Each value corresponded to the temperature when the Earth was assumed to be an equivalent blackbody emitter. Two values of longwave emittance were selected for each detector. These corresponded to the detector's response when in and out of direct solar radiation. The table on the following page gives the values of detector absorptance α_e and the two corresponding values of the detector response factor $(\alpha/\varepsilon)_e$ for each of the two detectors. The process for determining the ingression and egression points in the orbit, which indicate when to make the changeover in detector response

7

factors, is described in reference 4. The selection was based on the Sun zenith angle at the subsatellite point. The temperature change of the detectors was used as a backup indicator.

Detector	α_e	$(\alpha/\epsilon)_e$	
		Direct sunlight	No direct sunlight
White-coated	0.80	1.053	1.081
Black-coated	.94	1.000	1.021

When the spacecraft is not in direct sunlight, the last two terms of equations (4a) and (4b) are zero because only Earth-emitted radiation is being measured. For this condition, the ratio of the exitances in equations (4a) and (4b) should give the ratios of the detector's longwave response factors. When ratios of the computed exitances were plotted for the no-direct-sunlight condition, the values were found to be nearly constant and equal to the ratios as determined from the selected values of $(\alpha/\epsilon)_e$. This gives confidence in the technique for selecting values of longwave absorptance and emittance.

Detector Response to Shortwave Radiation

Based on flight test (refs. 2 and 9), the type of coatings used on the ESSA 7 detectors has a history of degrading. Ground tests at NASA Langley Research Center have shown the degradation was primarily a result of exposure to ultraviolet radiation. This degradation produces changes in the response of the detectors to shortwave radiation, and the white coatings were found to be much more vulnerable to degradation than the black coatings.

In the current analysis, the Sun is used as a calibration source to determine values of the shortwave-detector response factors. Just before the spacecraft exits from direct sunlight (egression), a detector measures longwave and direct solar radiation. After entry into total darkness, the detector measures longwave radiation only. If it is assumed that longwave radiation is constant for these two conditions, the difference in computed exitances for the white detector (using eq. (4a)) is

$$\Delta M_{d,w} = (\alpha/\epsilon)_{r,w} E_s$$

and similarly for the black detector

$$\Delta M_{d,b} = (\alpha/\epsilon)_{r,b} E_s$$

The procedure can also be followed at ingression, and thus, values of $(\alpha/\epsilon)_{r,w}$ and $(\alpha/\epsilon)_{r,b}$ can be inferred for the detectors twice during each orbit. A modified version of the preceding method was developed (ref. 4) which does not require the assumption that the longwave radiation remains constant for the period of the calculation. The values of $(\alpha/\epsilon)_r$ determined by this method for the two detectors are shown in figure 4. Values for the white-coated detectors are seen to vary about 25 percent over the data period, whereas values for the black-coated detector vary much less. These changes, although quite significant, are much smaller than those reported in reference 6 for the ITOS 1 instrument which changed its response by about 40 percent in a two-month period.

COMPUTATIONS

Irradiances

Values of emitted and reflected irradiances at the satellite were computed by equations (5a) and (5b) for each measurement in the edited data set. Values of solar irradiance E_s required in equation (5b) were computed by

$$E_s = H_s \left(\frac{1}{R}\right)^2 \left(\frac{\alpha}{\epsilon}\right)_s \frac{\sin \gamma}{\pi}$$

The value of the mean solar flux density H_s is 1353 W/m². Values of H_s used in previous studies have ranged from 1353 W/m² (ref. 6) to 1395 W/m² (ref. 1). A fairly recent experiment, reference 10, estimated a value for H_s of 1367 W/m².

The geometric shape factor $\sin \gamma/\pi$ relates the component of solar irradiance measured by the detector to the incoming solar flux density. A derivation of this shape factor is given in the appendix. The value of γ varied between 42° and 48° during the data period, and there was a corresponding change in the latitude—local-hour relationship. These variations reflect the departure from a truly Sun-synchronous orbit and the seasonal variation in the Sun's declination.

Flux Densities

Irradiances at the satellite were reduced to flux densities at an altitude of 30 km (top of the atmosphere) above the Earth (assumed radius = 6371 km) by the relationships

$$M_e = E_e/F \tag{6a}$$

$$M_r = E_r/F \tag{6b}$$

9

where F is the geometric shape factor. Values for the geometric shape factor
were calculated from the function derived in the appendix. It was assumed in
the derivation that the Earth's radiance field was Lambertian. It was shown
in references 11 and 12 that this assumption is valid for estimating emitted
flux densities. Reflected radiation is generally not diffuse at Sun zenith
angles greater than about 30°. However, most previous estimates of reflected
flux densities have been made using the diffuse assumption. The calculated
value of the shape factor was 0.2433 at a mean satellite altitude of 1450 km
and varied about ±2 percent with orbit altitude. These values were found to be
in very close agreement with values obtained using the methods of references 13
and 14.

Average Values of Flux Density and Albedo

Monthly averages of emitted flux density were derived from values obtained
from equation (6a) for 10°-latitude zones and for 10°-latitude-by-10°-longitude
regions for both the ascent and descent portions of the orbit. The average
local times corresponding to these averages of emitted flux densities can be
obtained from figure 1. For example, the average local times for ascent and
descent in the 0° to 10° zone are approximately 3 p.m. and 3 a.m. Monthly
averages of zonal and regional emitted flux densities based on the combined
data set were obtained by

$$\bar{M}_e = \frac{\bar{M}_{e,A} + \bar{M}_{e,D}}{2} \tag{7}$$

This averaging method precluded biasing the monthly averages for the combined
data set due to unequal sampling between ascent and descent.

Monthly averages of zonal and regional albedos were computed by

$$\bar{A} = \frac{(M_r)_{av}}{H_s(1/R)^2 \cos\!*\bar{\phi}} \tag{8}$$

where $(M_r)_{av}$ is the flux density in the zone or region obtained by averaging
the reflected flux densities of equation (6b). The denominator is the average
incident solar flux density corresponding to the measurements. It represents
the average reflected flux density that would be measured for an albedo of
unity. This incident solar flux density differs from that which would have
been obtained using $\cos\bar{\phi}$ because the Sun zenith varies over the detector
field of view. The difference is greatest at Sun zenith angles near 90°, as
can be seen in figure 5. This is because a large portion of the detector
field of view is not illuminated by the Sun. Average albedos were not
reported when the average zenith angle was greater than 90°.

10

Monthly averages of zonal and regional reflected flux densities were computed by

$$\bar{M}_r = \bar{M}_s \bar{A} \tag{9}$$

where $\bar{A}$ is obtained from equation (8). The monthly average of the incident solar flux density $\bar{M}_s$ for the zone or region is obtained by integrating incident solar flux density over the entire zone or region.

Monthly averages of zonal and regional net flux density were computed by

$$\bar{M}_n = \bar{M}_s - (\bar{M}_e + \bar{M}_r) = \bar{M}_s(1 - \bar{A}) - \bar{M}_e$$

Monthly averages of hemispherical and global emitted, reflected, and net flux densities were obtained by area weighting the monthly averages on zonal scales. For example, the monthly average of global emitted flux density is

$$\bar{M}_{e,G} = \frac{\displaystyle\sum_{i=1}^{18} (\bar{M}_{e,i}) a_i}{\displaystyle\sum_{i=1}^{18} a_i}$$

Monthly averages of hemispherical or global albedo are the ratios of the monthly averages of reflected flux to the monthly averages of incident solar flux. For instance, a monthly average of global albedo is

$$\bar{A}_G = \frac{\displaystyle\sum_{i=1}^{18} (\bar{M}_{r,i}) a_i}{\displaystyle\sum_{i=1}^{18} (\bar{M}_{s,i}) a_i}$$

Three-month averages of hemispherical and global flux densities are obtained by taking the average of the three separate monthly averages. The three-month average of hemispherical or global albedo is the ratio of the three-month average of reflected flux to the three-month average of incident solar flux. This aver-aging technique prevents biasing the three-month averages toward months with larger data sets.

RESULTS AND DISCUSSION

Global and Hemispherical Averages

ESSA 7.- Monthly and seasonal averages of hemispherical and global flux densities and albedo are given in table I for the ESSA 7 data period. Global emitted flux densities have a maximum and a minimum in October and January, respectively, with corresponding variations from the six-month average of about ±2 percent. Month-to-month changes in global emitted flux density during the winter months are due almost entirely to changes in emitted flux density in the Northern Hemisphere. Global albedo has a maximum, which occurs in November. The maximum variation from the average global albedo was less than 4 percent during the data period. This variation is due to changes in the albedo of the Southern Hemisphere. Averages of hemispherical net flux density are dominated by hemispherical solar flux density. For instance, albedo in the Northern Hemisphere has only a slight variation during the fall months, and emitted flux densities vary only about 4 W/m^2 for the three months. Net flux density, however, changes from 21 W/m^2 in September to -57 W/m^2 in November due to the seasonal decrease in hemispherical solar flux density.

Comparisons with other results.- Presented in table II are seasonal averages of global flux densities and albedos from ESSA 7 and three other sources (refs. 1, 8, and 15). Some global results from references 6 and 7 are also shown for comparison with appropriate ESSA 7 results from table I. Seasonal averages of the global emitted flux density from the reference sources are seen to be from 0 to 4 percent higher than those of ESSA 7, and there is up to 3 percent difference between averages within the three comparison sources. Combined averages for the two seasons are 225.5 W/m^2 for ESSA 7 and 231.8 W/m^2 for the reference sources. The corresponding blackbody temperatures are 251.1 K for ESSA 7 and 252.9 K for the references. The lower values obtained with ESSA 7 data are not surprising because references 1 and 5 indicate that a Sun-synchronous orbit with a 3-p.m. equator crossing should result in relatively low values of emitted flux density. Emitted flux density data of Nimbus 3 (ref. 7), which was in a 12-noon Sun-synchronous orbit, are higher than those of ESSA 7 by greater differences than those between ESSA 7 and the other three reference sources. The orbit of the NOAA 1 satellite (ref. 6) was nearly identical to that of ESSA 7, but the global average of emitted flux density from reference 6 is substantially greater than that of ESSA 7 for February. (See table I.) This may be due, in part, to assumptions necessary to determine degradation in the response of the NOAA 1 radiometers from in-flight data. The satellite was stabilized in three axes, and the detectors did not view the Sun directly. This meant that the Sun could not be used as an instrument calibration source as was done with ESSA 7.

12

Averages of global albedo from ESSA 7 are seen to be higher in the fall period and lower in the winter period than those of references 1, 8, and 15. Averages from these reference sources also show an increase in albedo from fall to winter whereas ESSA 7 data show a decrease. Very little difference is seen in albedo between the two periods shown from reference 7, and these values are both higher than the corresponding values for ESSA 7 in table I. Results of reference 6 show albedo values which are greater than those of all other sources discussed. Most of these differences are probably due to sampling differences imposed by the particular orbits, the majority of which were Sun synchronous.

Fall averages of global net flux density are in good agreement with those of references 8 and 15, but the winter averages agree better with results from reference 1. The large averages of emitted flux density and albedo obtained in reference 6 produced a loss in net flux density compared to a gain determined with ESSA 7 data.

Averages in 10°-Latitude Zones

Emitted flux density.- Monthly averages of zonal emitted flux density are given in figure 6. The largest month-to-month variations in emitted flux density are seen for the fall months in the Southern Hemisphere, and the smallest variations are seen for the winter months in the Southern Hemisphere. Comparisons of October and January averages for ESSA 7 with the results of reference 8 are given in figure 7. ESSA 7 results indicate that latitudinal variations in the equatorial zones are not as sharp as those seen in the results of reference 8, which included some data from scanning radiometers. The ESSA 7 detectors, which are rotating flat plates, generally smooth out the spatial variations in flux density more than scanning radiometers or wide-field-of-view (WFOV), fixed, horizontal flat plates. Averages of reference 8 are higher in the equatorial zones for both October and January, and agreement is reasonably good at latitudes above about 35°. An exception is seen for the Southern Hemisphere in January where results of reference 8 are significantly higher than those of the current study. October and January averages of emitted flux density are shown in figure 8 for the ascent and descent portions of the orbit. These generally show the ascent averages near the equator, which are taken near 3 p.m. local time, to be higher than the descent averages, which are taken at 3 a.m.

Albedo.- Monthly averages of zonal albedo are shown in figure 9. Latitudinal variability in the equatorial region is less in fall than in winter, and the differences between fall months in these regions are very small. Between fall months, differences in albedo near the poles in both hemispheres follow a seasonal pattern. That is, as the Sun moves southward from September to November, there is an increase in albedo in the Northern Hemisphere and a decrease in the Southern Hemisphere. In table I, note that the significant decrease in local albedo at high northern latitudes from December to February produces almost no change in hemispherical albedo. The opposite can be seen in the Southern Hemisphere. The accuracy of estimating albedo from WFOV measurements has always been a problem when the Sun is near the horizon, because the field of view of a WFOV detector includes some area which is illuminated by the Sun

13

and some which is in darkness. A parameter estimation technique described in reference 16 offers some promise of improvement in estimating reflected flux densities and albedos at high zenith angles. As with emitted flux density, differences in albedo between winter months near the South Pole are small. Comparisons of October and January averages of albedo between ESSA 7 and results of reference 8 are given in figure 10. Agreement, particularly near the equator, is seen to be very good.

Net flux density.- Monthly averages of zonal net flux density are presented in figure 11. The general shape of the monthly profiles and the month-to-month variations in net flux density are dominated by solar flux density. Maximum values of net flux density lag maximum solar flux density by a few degrees of latitude, except for September where net and solar flux densities are coincident in latitude. The accuracy of the variation near the poles is questionable due to the problem mentioned earlier in estimating albedo near the poles. Also, the poles are not illuminated in some months. Comparisons of October and January averages of net flux density between ESSA 7 and reference 8 are shown in figure 12. Agreement is very good in October and reasonably good in January.

Global Distributions

The monthly averages of flux densities and albedo in regions of 10° latitude by 10° longitude were used to generate global distributions (or maps) of radiation parameters. A cubic spline contour program was used with a spline tension factor of 2.5. The parametric cubic spline is generated by computing a polygonal contour through the defined grid and then generating the splined contour by using the polygonal contour length (normalized to one) as the independent variable. Contour slopes are matched when a contour closes. ESSA 7 results are presented in figures 13 to 15.

Contour maps of emitted flux density and albedo, presented in figures 16 and 17, show comparisons of results from ESSA 7 (Sept. 1968) with results from Nimbus 6 (Aug. 1975). The Nimbus 6 values are previously unpublished results obtained by the authors. The data are from the wide-field-of-view detector of the Earth radiation budget (ERB) experiment on the Nimbus 6 satellite. (See ref. 17.) The contour technique is the same as that used on the ESSA 7 data.

Emitted flux density.- Global maps of emitted flux density are shown in figure 13 for October and January. It can be seen that the ESSA 7 detectors identified significant structure in emitted flux density in a tropical zonal band extending about $\pm25^{\circ}$ in latitude. Longitudinal gradients in this zonal band are, in some areas, as great as latitudinal gradients. For instance, there is a strong positive gradient extending westward from a low over western South America to a high over the Pacific Ocean. The influence of the structural band extends northward in October to include some of North America and the Mediterranean Sea, but the limit of the northward influence in January is below the tropic of Cancer. In this band, highs are generally centered over oceans and

lows over land, usually coinciding with minimum and maximum regions of cloudiness, respectively. Photographs taken by Vidicon cameras on the ESSA 7 satellite show a nearly cloud-free region in October corresponding to the indicated high in emitted flux density centered over southern Saudi Arabia, and the January photographs showed a buildup of cloudiness in that region.

Comparisons of emitted flux density are given in figure 16. The structure in the zonal band of influence is quite similar for the two data sets. The structure is more detailed for the Nimbus 6 data, however. Some of this may be due to the differences between September and August, but it is probably also due to the higher resolution of the flat-plate detector on Nimbus 6. The magnitudes of the Nimbus 6 data are also higher. This may be due to the difference in local time when the two satellites cross the equator. The Nimbus 6 orbit was Sun synchronous with a 12-noon northward equatorial crossing.

Albedo.- Global maps of albedo for October and January are shown in figure 14. Comparison of figure 14 with figure 13 shows that areas of low albedo, in general, correspond to areas of high emitted flux density, and vice versa. This is more apparent in January when the longitudinal structure in the tropics is more clearly defined. It is interesting that the decrease in emitted flux density from October to January over southern Saudia Arabia does not have a corresponding increase in albedo, which is as sharp in detail. This may be due, in part, to the southerly shift of the band of longitudinal variability. Outside this band, latitudinal variability overrides longitudinal variability. As with emitted flux density, the comparison maps of figure 17 show remarkable similarities between the September albedos from ESSA 7 and those for August from Nimbus 6. For instance, the highs in albedo over Africa are almost identical in shape for both data sets, and the contours on the east and west sides of South America are nearly the same for both data sets.

Net flux density.- Global maps of net flux density for October and January are presented in figure 15. The dominant influence of solar flux density on the global distribution of net flux density can be seen in figure 15 where the width of the zone showing significant longitudinal variations is more narrow than for either emitted flux or albedo.

CONCLUDING REMARKS

The ESSA 7 data set is an important part of the Earth radiation measurements of the late 1960's. For the six months of data analyzed, the time and spatial coverage was quite good. Results are enhanced by using the in-flight calibration technique developed in NASA CR-132623. The values of emitted flux density are lower and the values of albedo are higher than most corresponding values found in previous radiation budget studies. This may be due, in part, to the 3-p.m. Sun-synchronous orbit of ESSA 7. Latitudinal gradients dominate the spatial distributions of emitted flux density and albedo near the poles. Significant longitudinal gradients, however, were identified in a tropical zone

extending $\pm 25°$ in latitude. Highs in emitted flux density occurred mostly over oceans and lows over land, while the opposite was found for albedo. Monthly changes in zonal and hemispherical net flux densities are dominated by changes in solar flux density.

Langley Research Center
National Aeronautics and Space Administration
Hampton, VA 23665
March 7, 1979

16

APPENDIX

GEOMETRIC SHAPE FACTORS FOR THE ESSA 7 DETECTORS

Upwelling Earth Radiation

Let the radiance be Lambertian (diffuse) everywhere on a spherical surface above the Earth, and let the flux density M be a function of longitude λ and latitude θ. An increment of irradiance at a satellite due to radiation from an increment of area on the surface can be written

$$dE = \frac{1}{\pi} M(\lambda,\theta) \cos \xi \, d\omega$$

where ξ is the angle which the incoming ray makes with the normal to the detector surface and $d\omega$ is the solid angle at the detector subtended by the increment of area. The total irradiance due to the Earth region within the detector field of view (FOV) is given by

$$E = \frac{1}{\pi} \int_{FOV} M(\lambda,\theta) \cos \xi \, d\omega$$

If the flux density is assumed to be uniform over the detector field of view, the irradiance can be expressed as a product of the flux density and a geometric shape factor F. That is,

$$E = MF$$

where the geometric shape factor is given by

$$F = \frac{1}{\pi} \int_{FOV} \cos \xi \, d\omega \tag{A1}$$

Figure 18 illustrates the geometry of the ESSA 7 detector. The rotation angle β of the detector was in a plane normal to the surface of the Earth. In this spherical coordinate system,

$$\xi = \eta$$

and

$$d\omega = \cos \eta \, d\eta \, d\beta$$

Thus, equation (A1) can be written

$$F = \frac{4}{\pi} \int_0^{\eta_{max}} \int_0^{\beta(\eta)_{max}} \cos^2 \eta \, d\beta \, d\eta$$

Integrating over β and expressing β in terms of η,

$$\beta_{max}(\eta) = \cos^{-1} \left(\frac{\cos \eta_{max}}{\cos \eta} \right)$$

Since the detector rotates through π radians while β goes from 0 to $\beta_{max}(\eta)$, the shape factor can be expressed as

$$F = \frac{4}{\pi^2} \int_0^{\eta_{max}} \cos^2 \eta \, \cos^{-1} \left(\frac{\cos \eta_{max}}{\cos \eta} \right) d\eta \qquad (A2)$$

where the unrestricted view angle

$$\eta_{max} \equiv \sin^{-1} \left(\frac{R + h_0}{R + h} \right)$$

The integral (eq. (A2)) was evaluated numerically over the range of η_{max} which corresponded to the variation in orbit altitude. The value of η_{max} is 55° at the mean satellite altitude of 1450 km.

18

APPENDIX

Direct Solar Radiation

The solar flux at the Earth can be expressed as

$$H_S \left(\frac{1}{L}\right)^2$$

where H_S is the solar flux density at the mean distance of the Sun from the Earth and L is the actual distance normalized by the mean distance.

Now, let a flat-plate detector have an absorptance α and an emittance ε relative to solar radiation. If the plate is rotated through an incremental angle $d\beta$ about an axis which is inclined to the Sun's rays by an angle γ, an increment of irradiance can be expressed as

$$dE_S = H_S \left(\frac{1}{L}\right)^2 (\alpha/\varepsilon)_S \sin \gamma \cos \beta \, d\beta$$

During each revolution, the plate is exposed to sunlight half the time, and the irradiance is given by

$$E_S = H_S \left(\frac{1}{L}\right)^2 (\alpha/\varepsilon)_S \frac{\sin \gamma}{2\pi} \int_{-\pi/2}^{\pi/2} \cos \beta \, d\beta$$

or

$$E_S = H_S \left(\frac{1}{L}\right)^2 (\alpha/\varepsilon)_S \frac{\sin \gamma}{\pi}$$

The factor $\sin \gamma / \pi$ can be thought of as a geometric shape factor for a rotating flat plate exposed to direct solar radiation.

REFERENCES

1. Vonder Haar, Thomas Henry: Variations of the Earth's Radiation Budget. Ph. D. Thesis, Univ. of Wisconsin, 1968.

2. GCA Technology Division: The Reduction, Analysis and Interpretation of Radiation Balance Measurements from ESSA Weather Satellites. GCS-TR-69-17-G (ESSA Contract No. E-119-68(N)), GCA Corp., Apr. 1970.

3. MacDonald, Torrence H.: Data Reduction Processes for Spinning Flat-Plate Satellite-Borne Radiometers. ESSA Tech. Rep. NESC 52, U.S. Dep. Commer., July 1970.

4. House, Frederick B.: An Investigation of ESSA VII Radiation Data for Use in Long-Term Earth Energy Experiments. NASA CR-132623, [1975].

5. Astling, Elford G.; and Horn, Lyle H.: An Analysis of Diurnal Variations in TIROS II Radiation Data. Annual Rep. (Grant WBG-10), Dep. Meteorology, Univ. of Wisconsin, Oct. 1964, pp. 0-24.

6. Flanders, Donald H.; and Smith, William L.: Radiation Budget Data From the Meteorological Satellites, ITOS 1 and NOAA 1. NOAA Tech. Memo. NESS 72, Aug. 1975.

7. Raschke, Ehrhard; Vonder Haar, Thomas H.; Bandeen, William R.; and Pasternak, Musa: The Annual Radiation Balance of the Earth-Atmosphere System During 1969-70 From Nimbus 3 Measurements. J. Atmos. Sci., vol. 30, no. 3, Apr. 1973, pp. 341-364.

8. Ellis, James S.; and Vonder Haar, Thomas H.: Zonal Average Earth Radiation Budget Measurements From Satellites for Climate Studies. NASA CR-149319, 1976.

9. House, Frederick Bishop: The Radiation Balance of the Earth From a Satellite. NASA CR-76422, 1965.

10. Duncan, Charles H.; Harrison, Royal G.; Hickey, John R.; Kendall, James M., Jr.; Thekaekara, Matthew P.; and Willson, Richard C.: Rocket Calibration of the Nimbus 6 Solar Constant Measurements. NASA TM X-71305, 1977.

11. Weaver, W. L.: Simulation Study of a Method for Analyzing Wide Field of View Radiometer Measurements From Satellites and Some Analysis of ESSA 7 Data. Third National Aeronautics and Space Administration Weather and Climate Program Science Review, Earl R. Kreins, ed., NASA CP-2029, 1977, pp. 305-309.

12. Weaver, William L.; and Green, Richard N.: Analysis of Simulated Measurements of Earth Emitted Radiation Using Geometric Shape Factors and Some Results From Analysis of ESSA 7 and Nimbus 6 Data. NASA paper presented at Third Conference on Atmospheric Radiation (Davis, Calif.), June 28-30, 1978.

13. Stevenson, J. A.; and Grafton, J. C.: Radiation Heat Transfer Analysis for Space Vehicles. ASD Tech. Rep. 61-119, Pt. I, U.S. Air Force, Dec. 1961.

14. Turner, Richard E.: Solutions and Methods of Solutions for Problems Encountered in the Thermal Design of Spacecraft. M.S. Thesis, Virginia Polytechnic Institute, 1964.

15. Vonder Haar, Thomas H.; and Suomi, Verner E.: Measurements of the Earth's Radiation Budget From Satellites During a Five-Year Period. Part I: Extended Time and Space Means. J. Atmos. Sci., vol. 28, no. 3, Apr. 1971, pp. 305-314.

16. Green, Richard N.: Simulation Studies of Wide and Medium Field of View Earth Radiation Data Analysis. NASA TP-1182, 1978.

17. Smith, W. L.; Hickey, J.; Howell, H. B.; Jacobowitz, H.; Hilleary, D. T.; and Drummond, A. J.: Nimbus-6 Earth Radiation Budget Experiment. Appl. Opt., vol. 16, no. 2, Feb. 1977, pp. 306-318.

TABLE I.- MONTHLY AND SEASONAL AVERAGES OF RADIATION PARAMETERS FOR ESSA 7 DATA PERIOD (SEPT. 1968 THROUGH FEB. 1969)

Period*	Solar flux density, W/m^2	Emitted flux density, W/m^2	Reflected flux density, W/m^2	Net flux density, W/m^2	Albedo
Sept.:					
NH	351.1	228.9	100.9	21.3	0.287
SH	317.8	223.1	97.4	-2.7	.306
G	334.4	226.0	99.2	9.2	.297
Oct.:					
NH	288.2	231.8	83.0	-26.6	0.288
SH	392.3	229.3	128.2	34.8	.327
G	340.2	230.5	105.6	4.1	.310
Nov.:					
NH	236.1	225.0	68.5	-57.4	0.290
SH	455.1	231.6	148.8	74.7	.327
G	345.6	228.3	108.7	8.6	.315
Sept.-Oct.-Nov.:					
NH	291.8	228.6	84.0	-20.8	0.288
SH	388.4	228.0	124.8	35.6	.321
G	340.1	228.3	104.4	7.4	.307
Dec.:					
NH	211.9	220.6	59.5	-68.2	0.281
SH	486.0	228.3	152.7	105.0	.314
G	349.0	224.5	106.1	18.4	.304
Jan.:					
NH	224.0	213.0	52.6	-51.6	0.279
SH	473.7	228.3	144.6	100.8	.305
G	348.9	220.7	103.6	24.6	.297
Feb.:					
NH	268.1	216.0	75.0	-22.9	0.280
SH	425.6	229.2	126.8	69.6	.298
G	346.9	222.6	100.9	23.4	.291
Dec.-Jan.-Feb.:					
NH	234.7	216.5	65.7	-47.5	0.280
SH	461.8	228.6	141.4	91.8	.306
G	348.2	222.6	103.5	22.1	.297

*NH, Northern Hemisphere; SH, Southern Hemisphere; and G, Global.

TABLE II.- COMPARISON OF ESSA 7 GLOBAL RESULTS WITH OTHER DATA

| Source | Satellite orbit | Data period | | Average on global scale | | |
		Months	Years	Emitted flux density, W/m^2	Net flux density, W/m^2	Albedo
Present analysis	ESSA 7 3-p.m.[1] SS[2] orbit	Sept., Oct., Nov.	1968	228.3	7.4	0.307
		Dec., Jan., Feb.	1968-69	222.6	22.1	0.297
Reference 1	Several satellites, different orbits	Sept., Oct., Nov.	1963 1964 1965	237.1	14.0	0.280
		Dec., Jan., Feb.	1960-61 1961-62 1962-63 1963-64 1964-65	223.1	20.9	0.310
Reference 15	Several satellites, different orbits	Sept., Oct., Nov.	1963 1964 1965	237.1	7.0	0.280
		Dec., Jan., Feb.	1963-64 1964-65 1965-66	230.1	7.0	0.310
Reference 8	Several satellites, different orbits	Sept., Oct., Nov.	1964 1968 1969	233.1	6.3	0.301
		Dec., Jan., Feb.	1964-65 1968-69	230.2	10.4	0.311
Reference 7	Nimbus 3, 12-noon SS orbit	Oct. 3-17	1969	242.7	4.2	0.282
		Jan. 21 - Feb. 3	1970	235.0	16.0	0.283
Reference 6	NOAA 1, 3-p.m. SS orbit	Feb. 18 - Mar. 16	1971	247.0	-12.1	0.351

[1]Local time for ascent crossing at equator.
[2]SS, Sun synchronous.
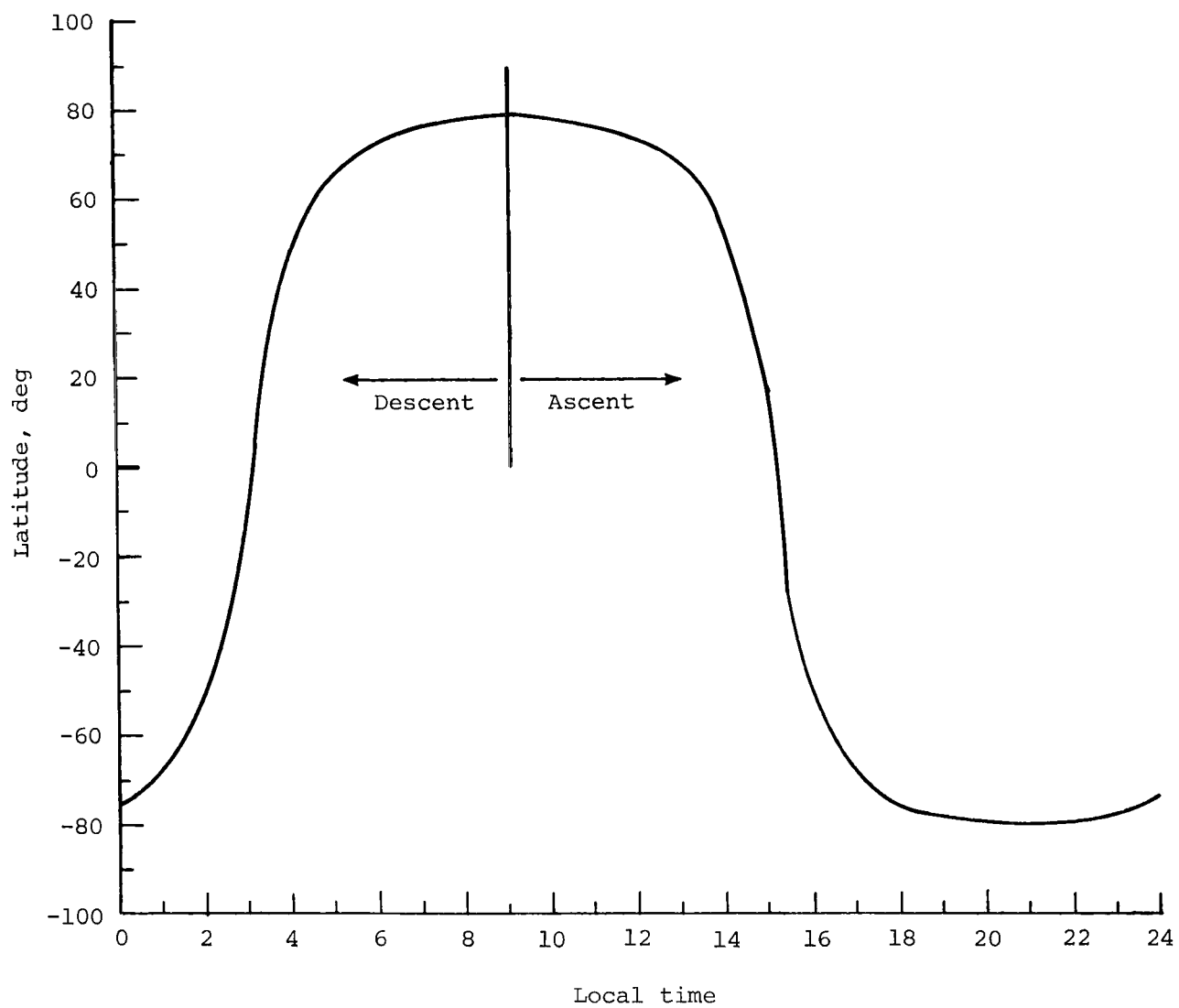
Figure 1.- Average local time as function of spacecraft latitude.
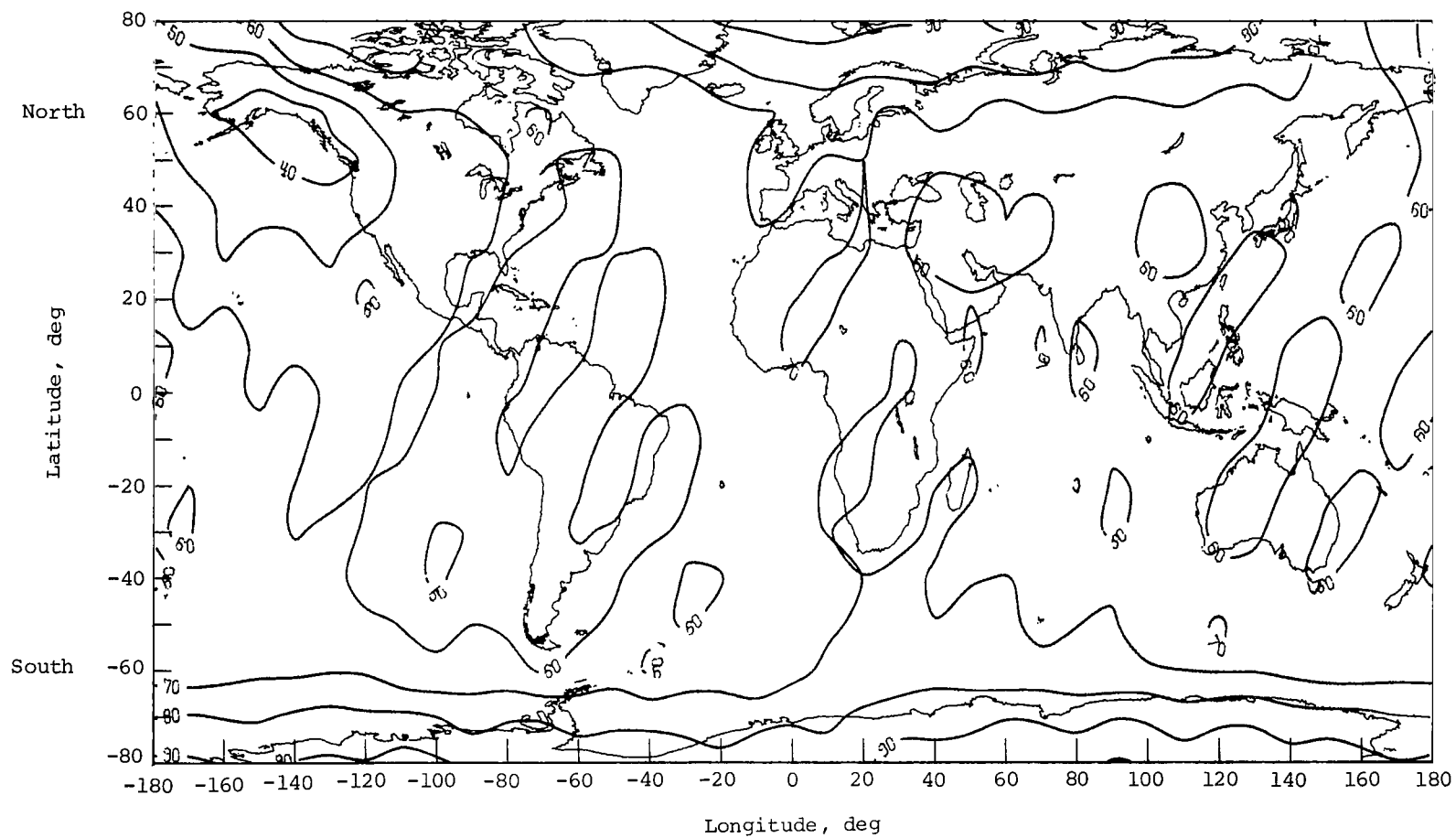
(a) Ascent.

Figure 2.- Spatial distribution of edited data for October 1968. Based on number of measurements in 10° × 10° regions.
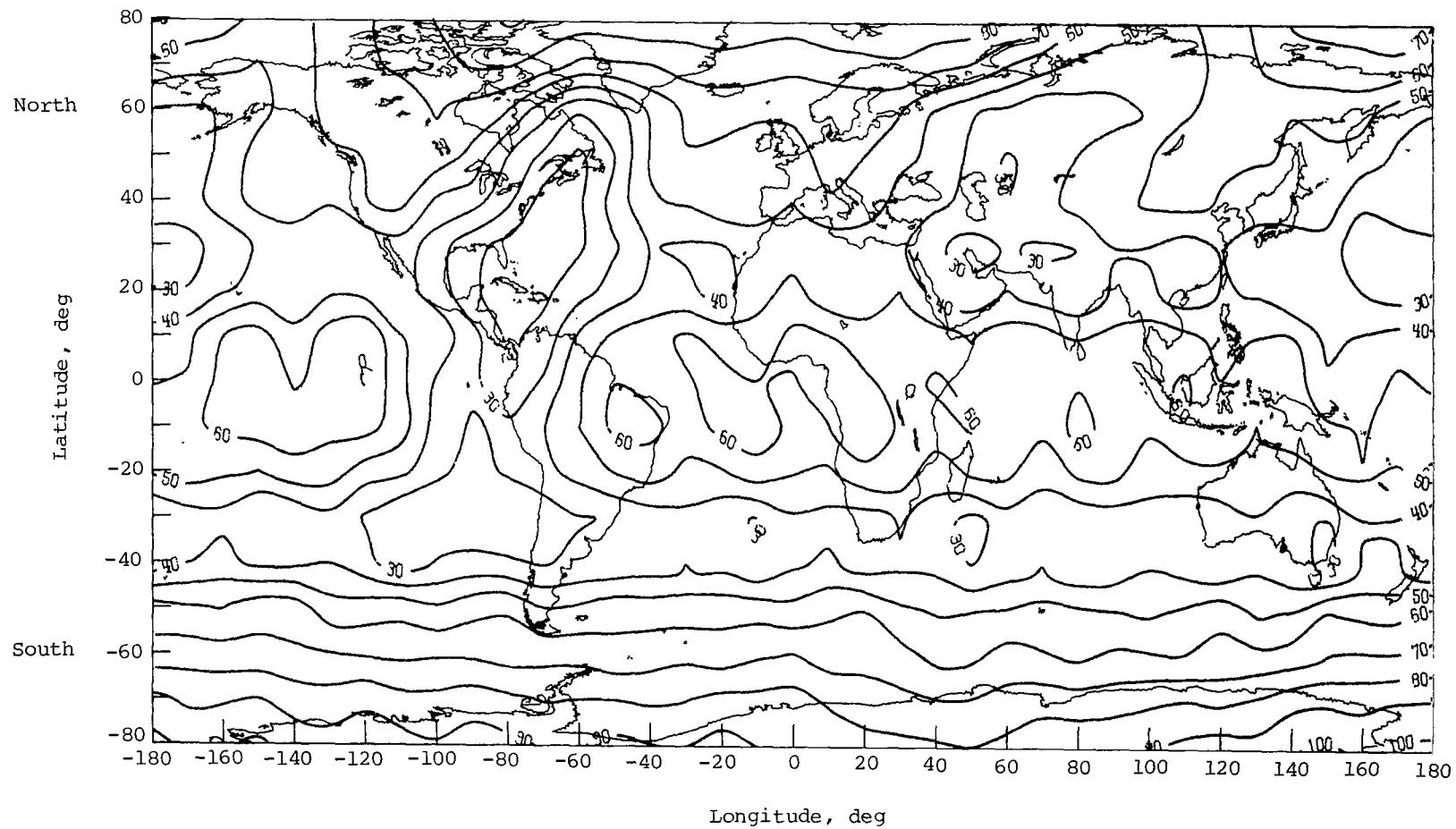
(b) Descent.

Figure 2.- Concluded.
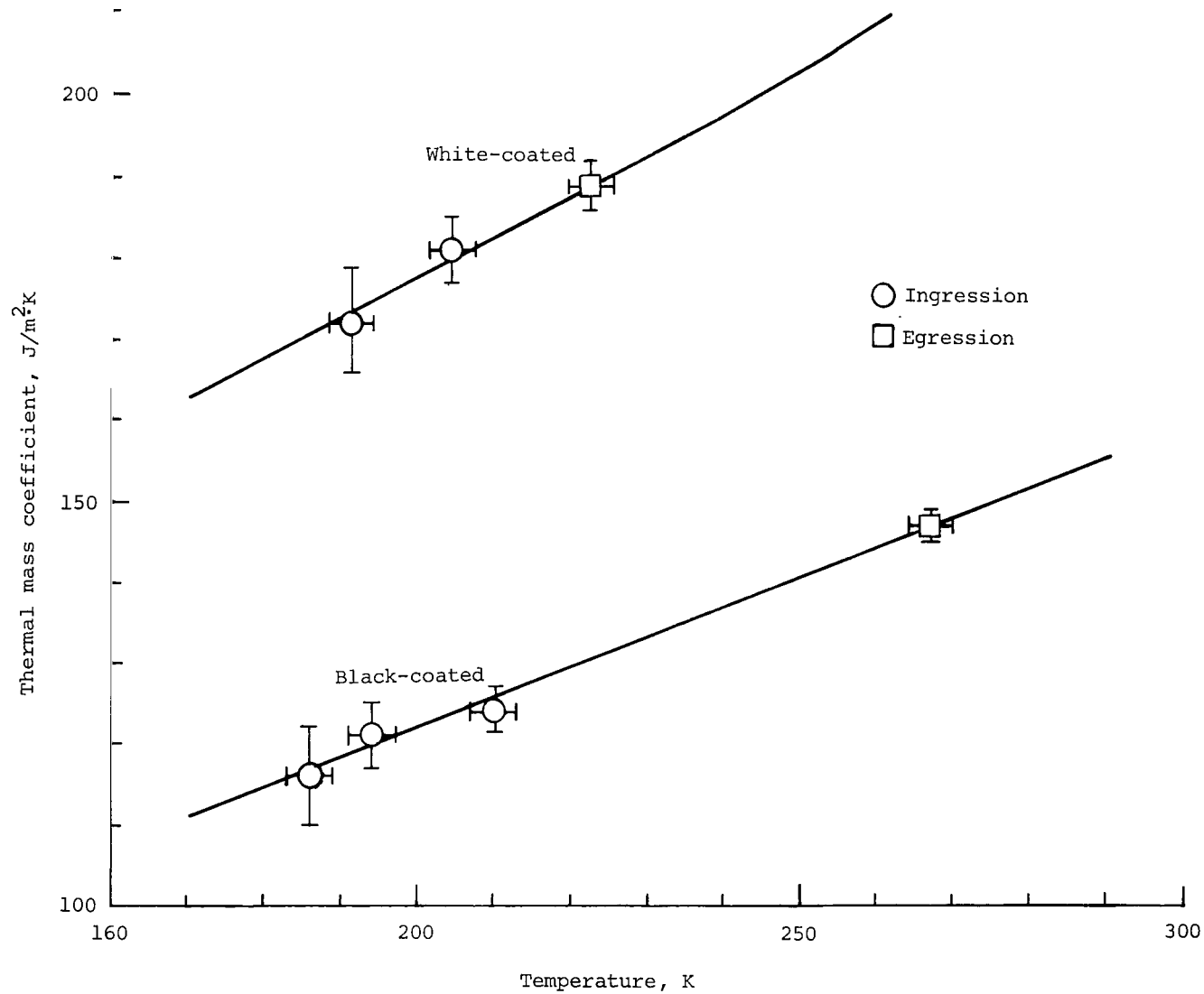
Figure 3.- Variation of thermal mass coefficient with detector temperature for white- and black-coated radiometers.
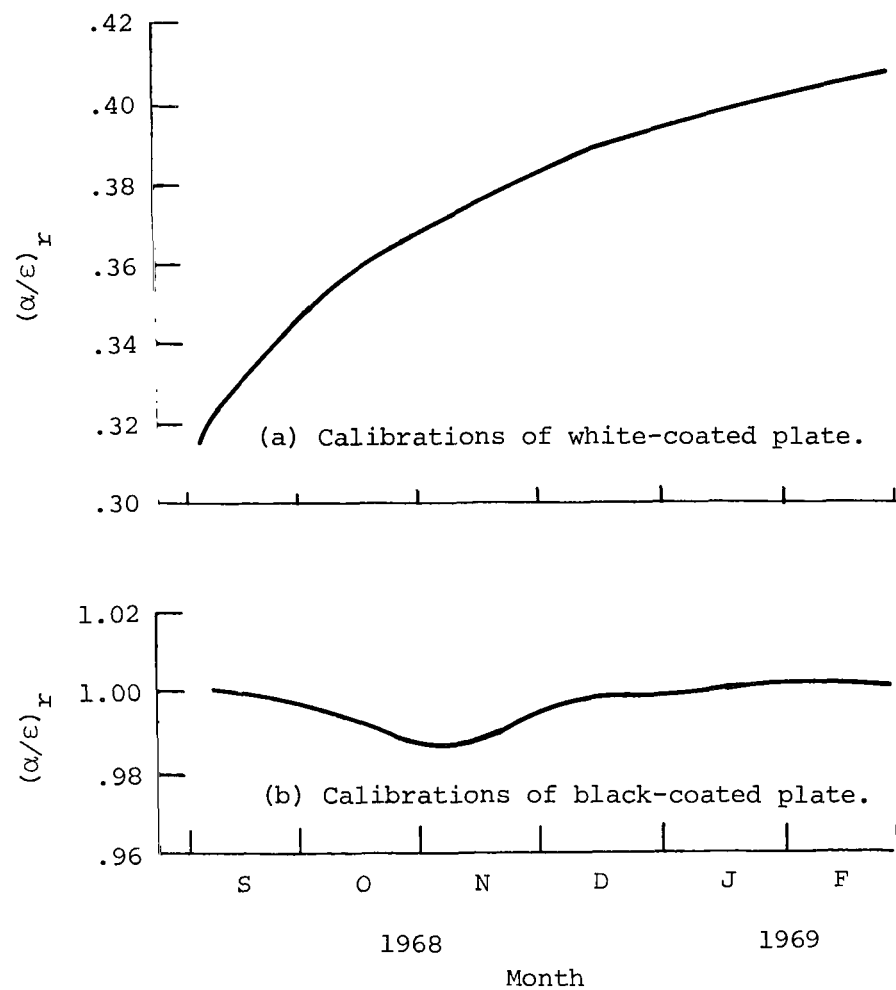
Figure 4.- Values of shortwave detector response factor $(\alpha/\epsilon)_r$ for plate radiometers on ESSA 7.
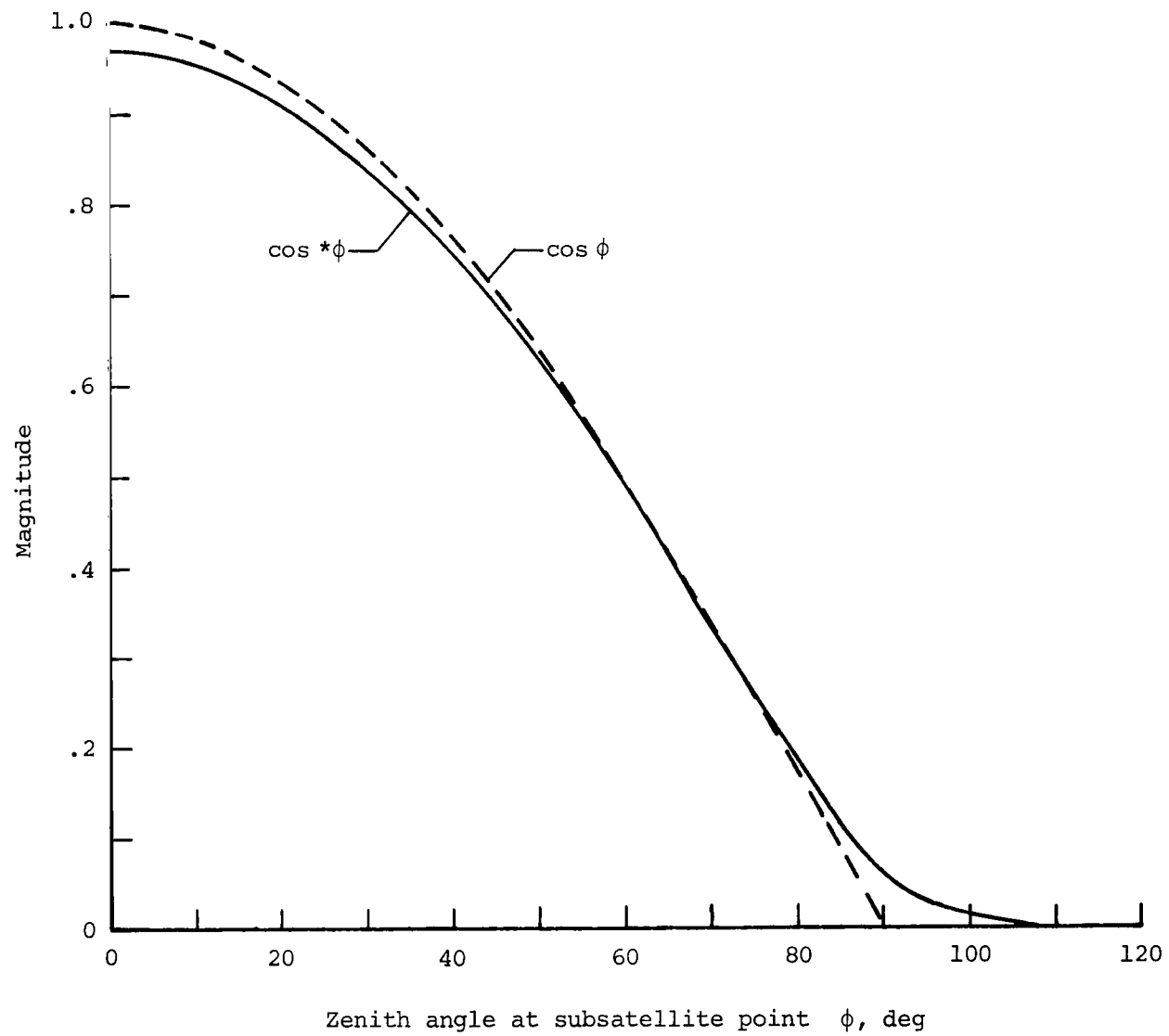
Figure 5.- Comparison of cos *φ with cos φ.
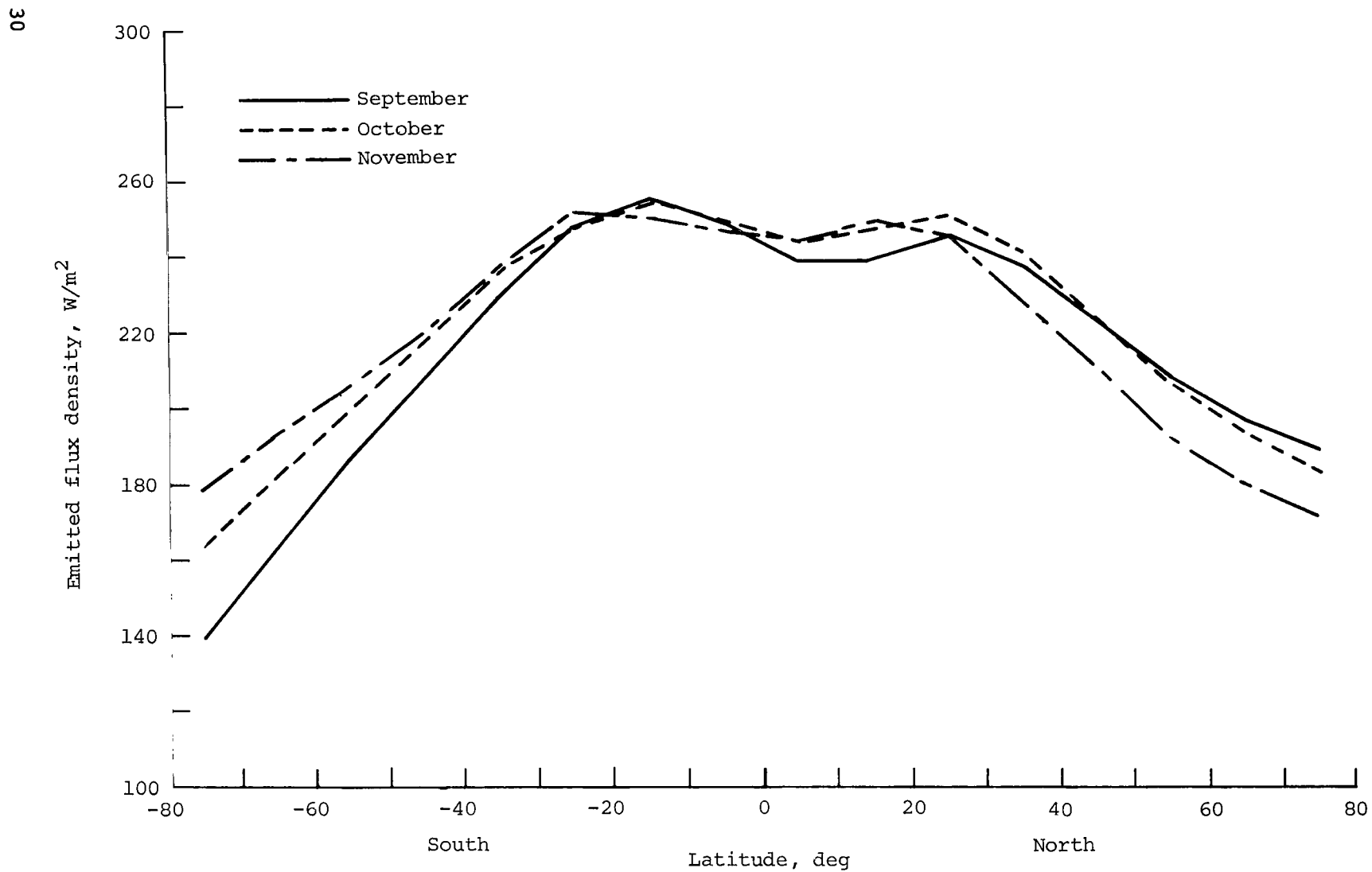
(a) September, October, November.

Figure 6.- Monthly averages of zonal emitted flux density for each month analyzed.
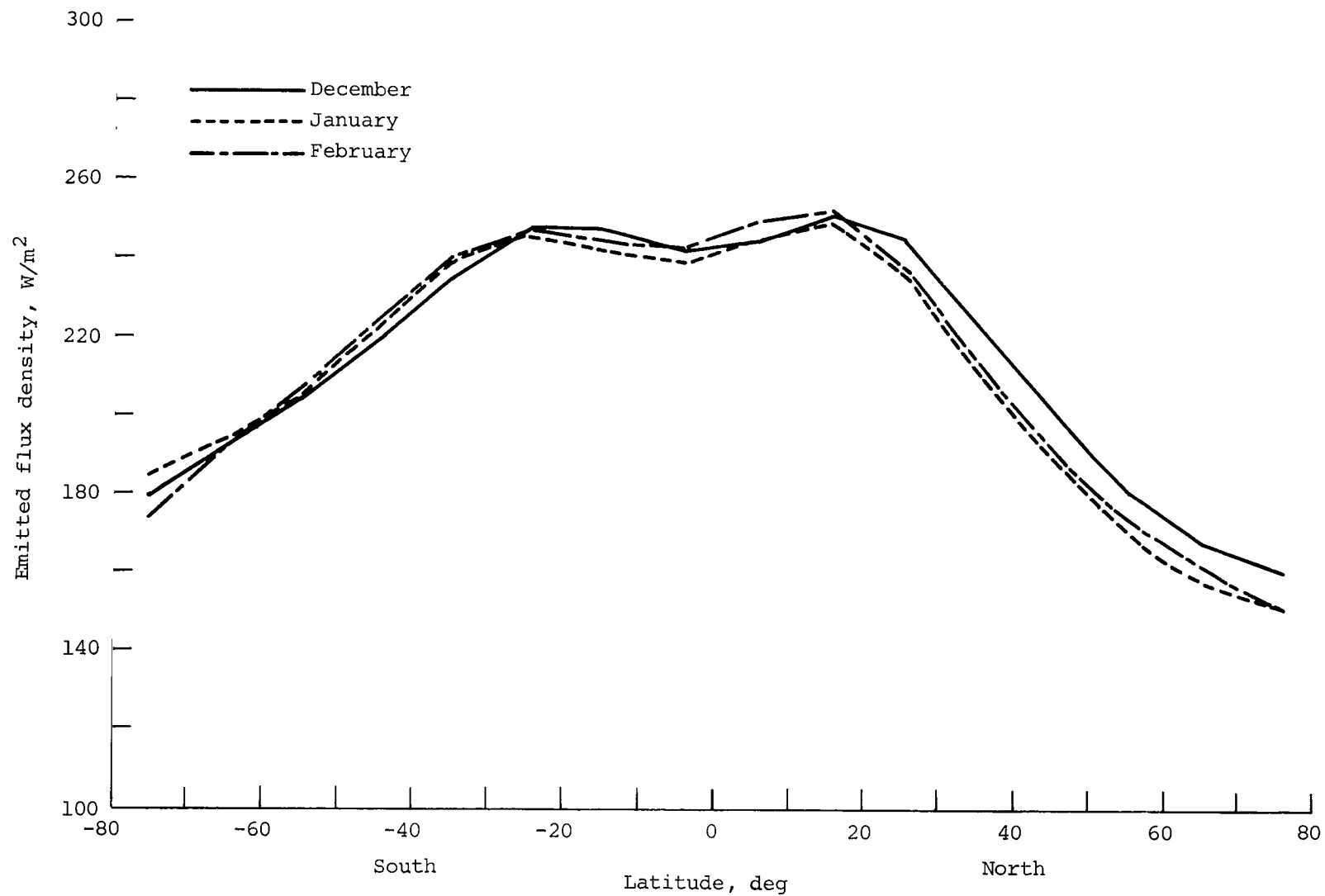
(b) December, January, February.

Figure 6.- Concluded.

Global mean, W/m^2

———— Current work   230.5
— — — Reference 8   236.0
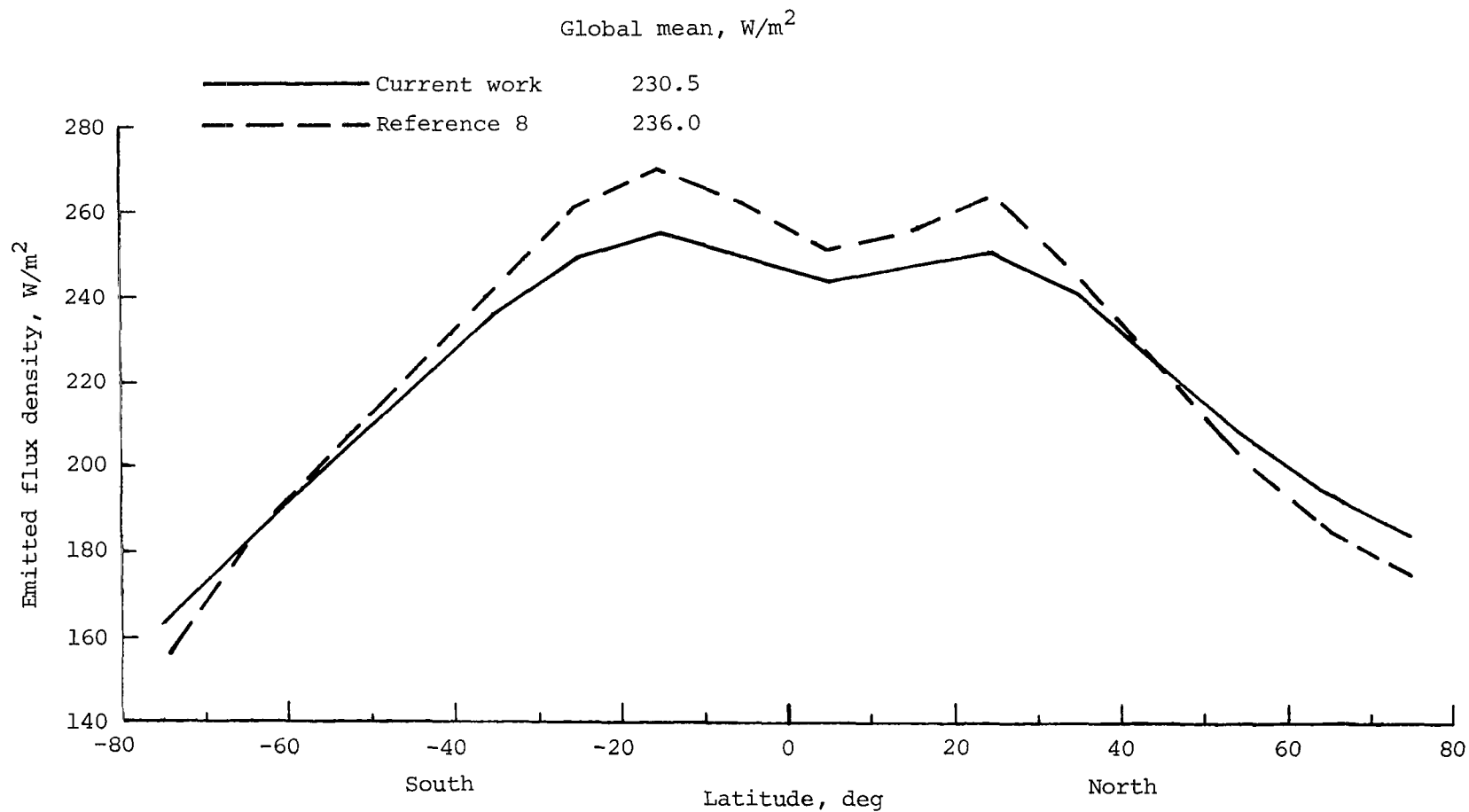
(a) October.

Figure 7.- Comparison of emitted flux density for ESSA 7 with the results
of reference 8.

Global mean, W/m^2

——— Current work   220.6

— — — Reference 8   231.2
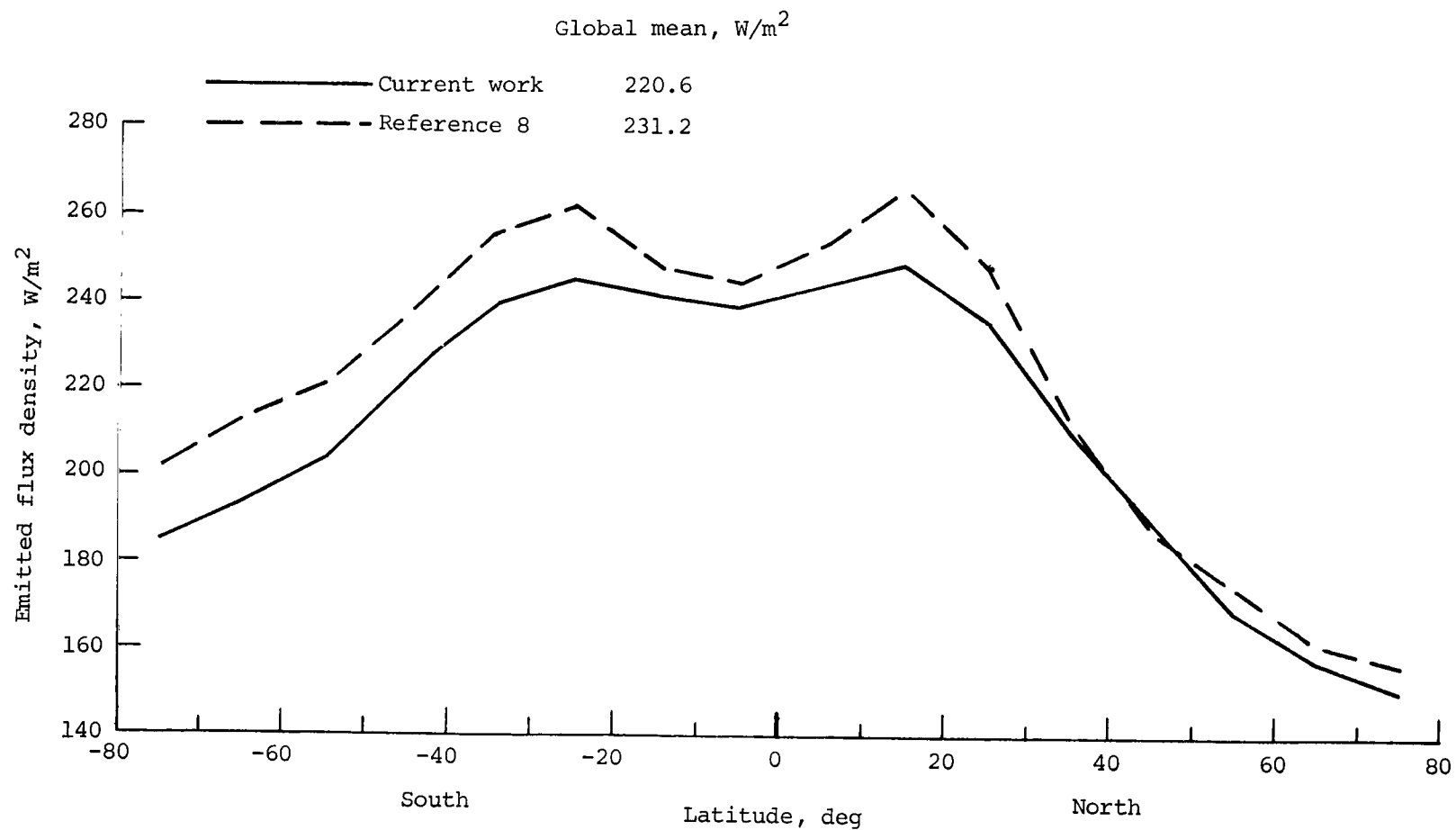
(b) January.

Figure 7.- Concluded.
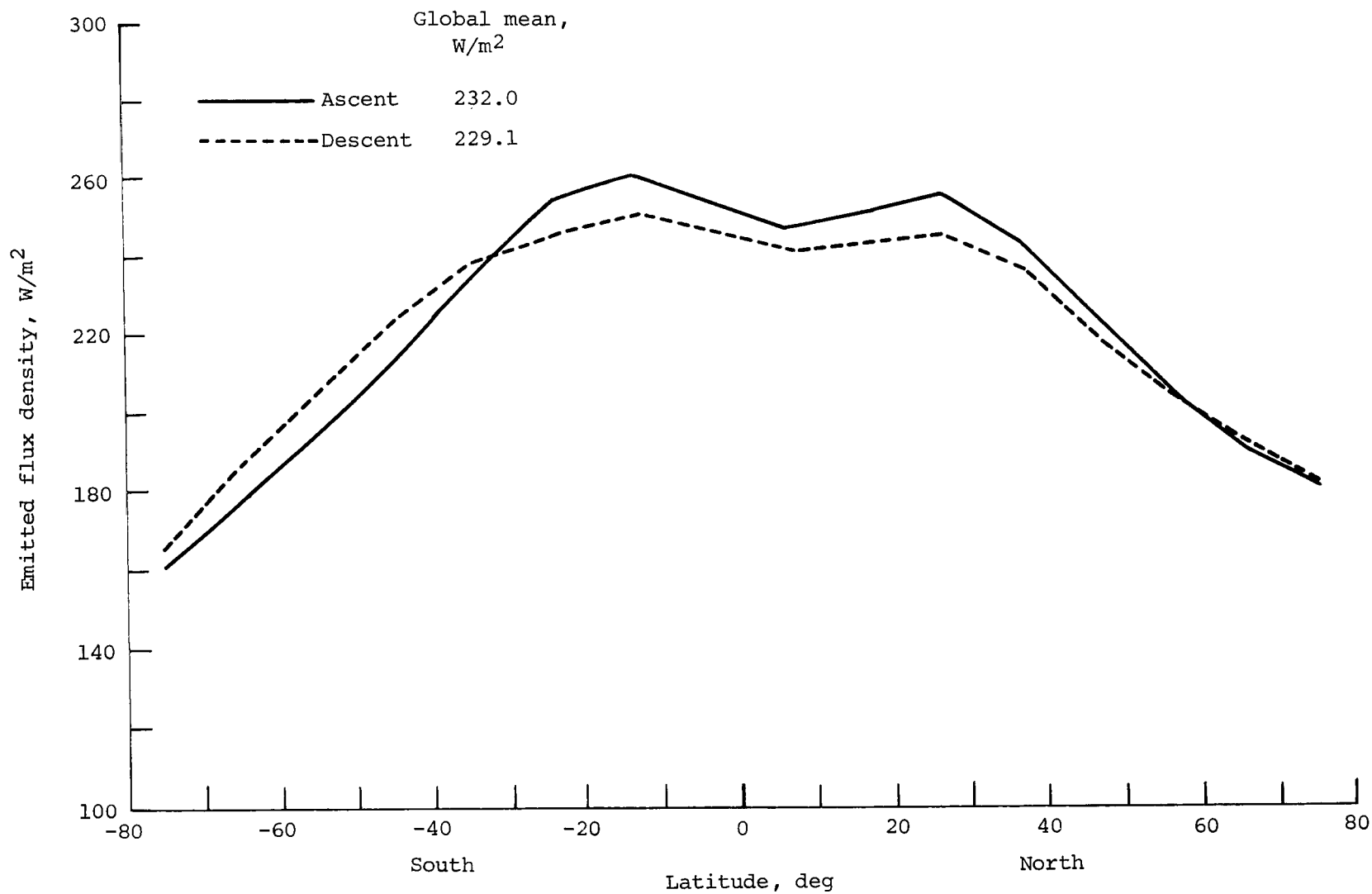
(a) October.

Figure 8.- Typical plots of zonal emitted flux density for ascent and descent.
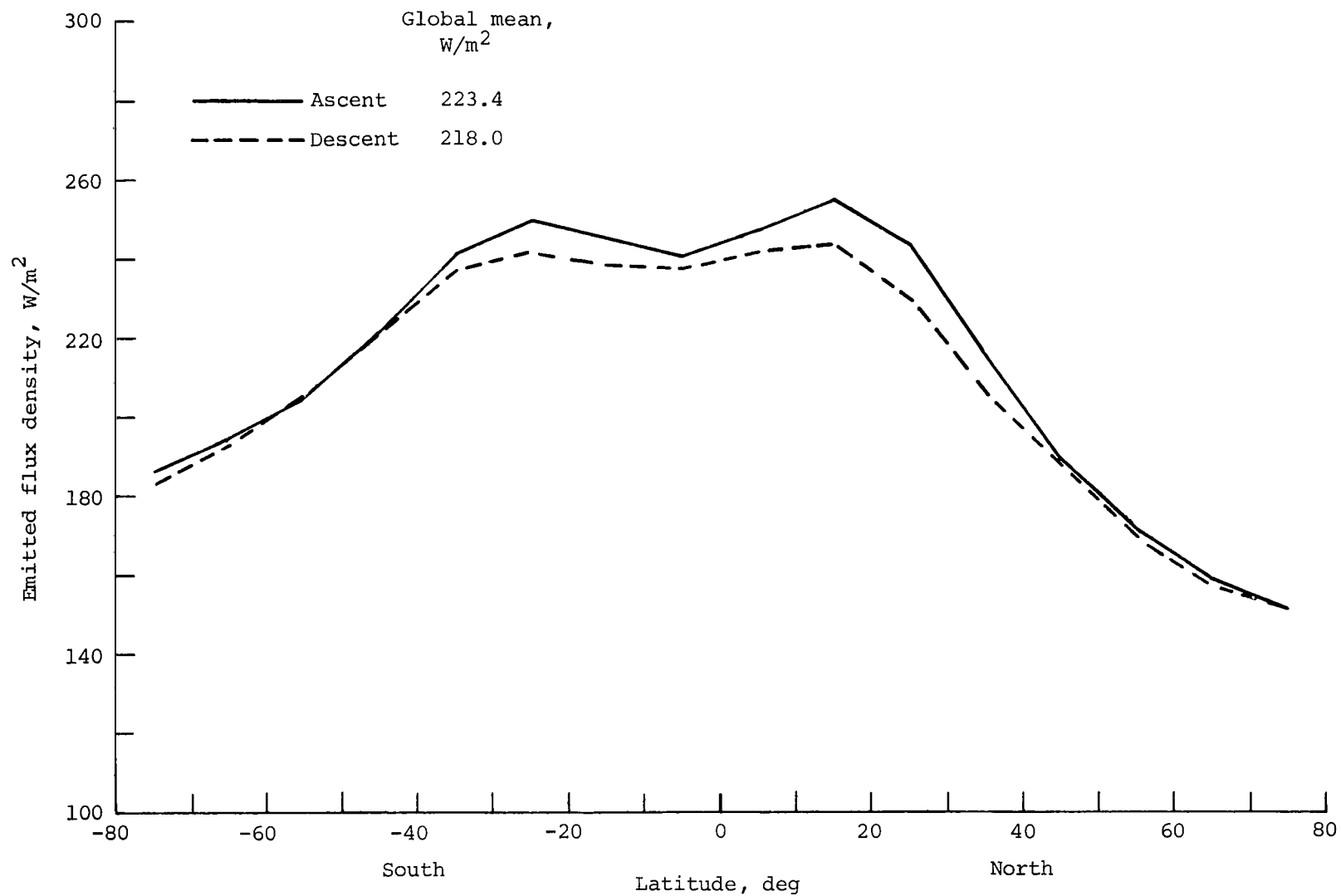
(b) January.

Figure 8.- Concluded.
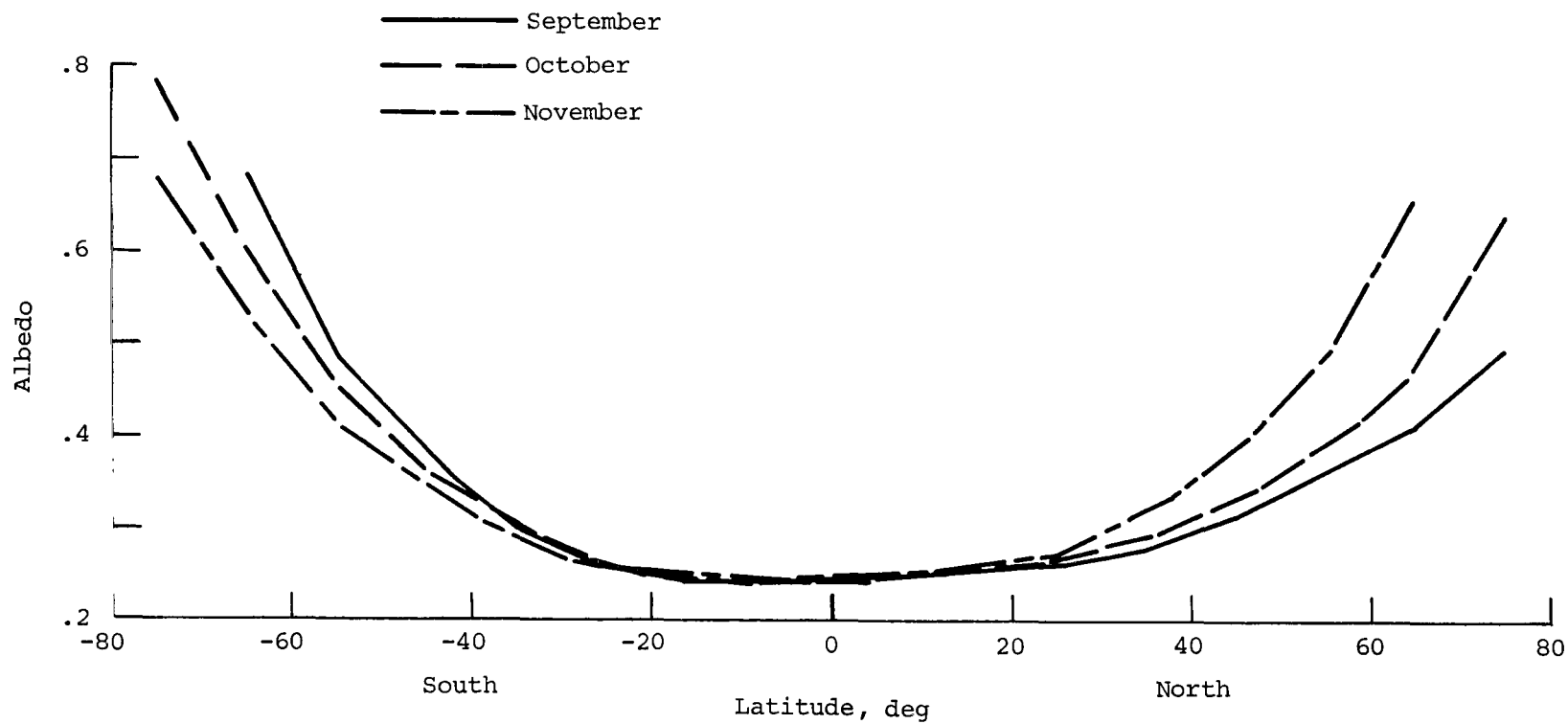
(a) September, October, November.

Figure 9.- Monthly averages of zonal albedo for each month analyzed.
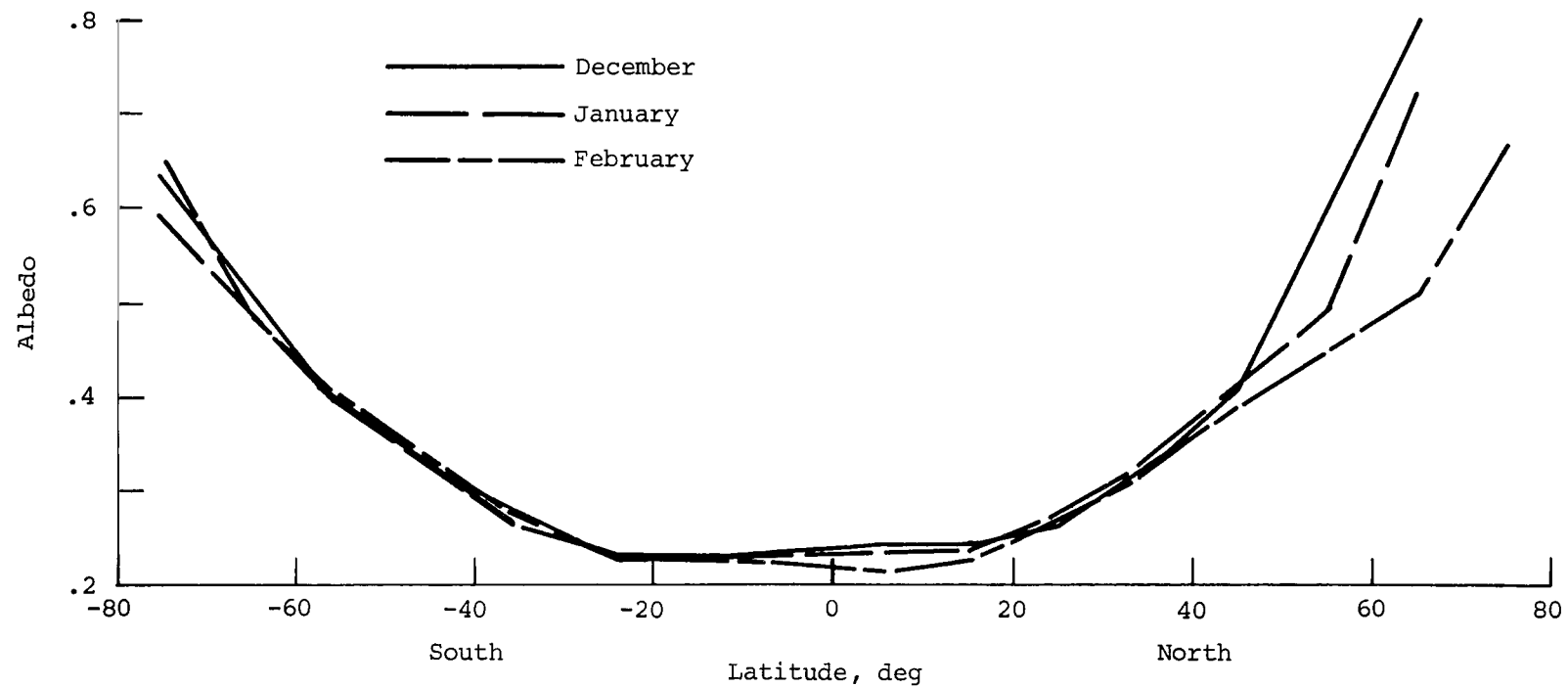
(b) December, January, February.

Figure 9.- Concluded.

Global mean

Current work   0.311
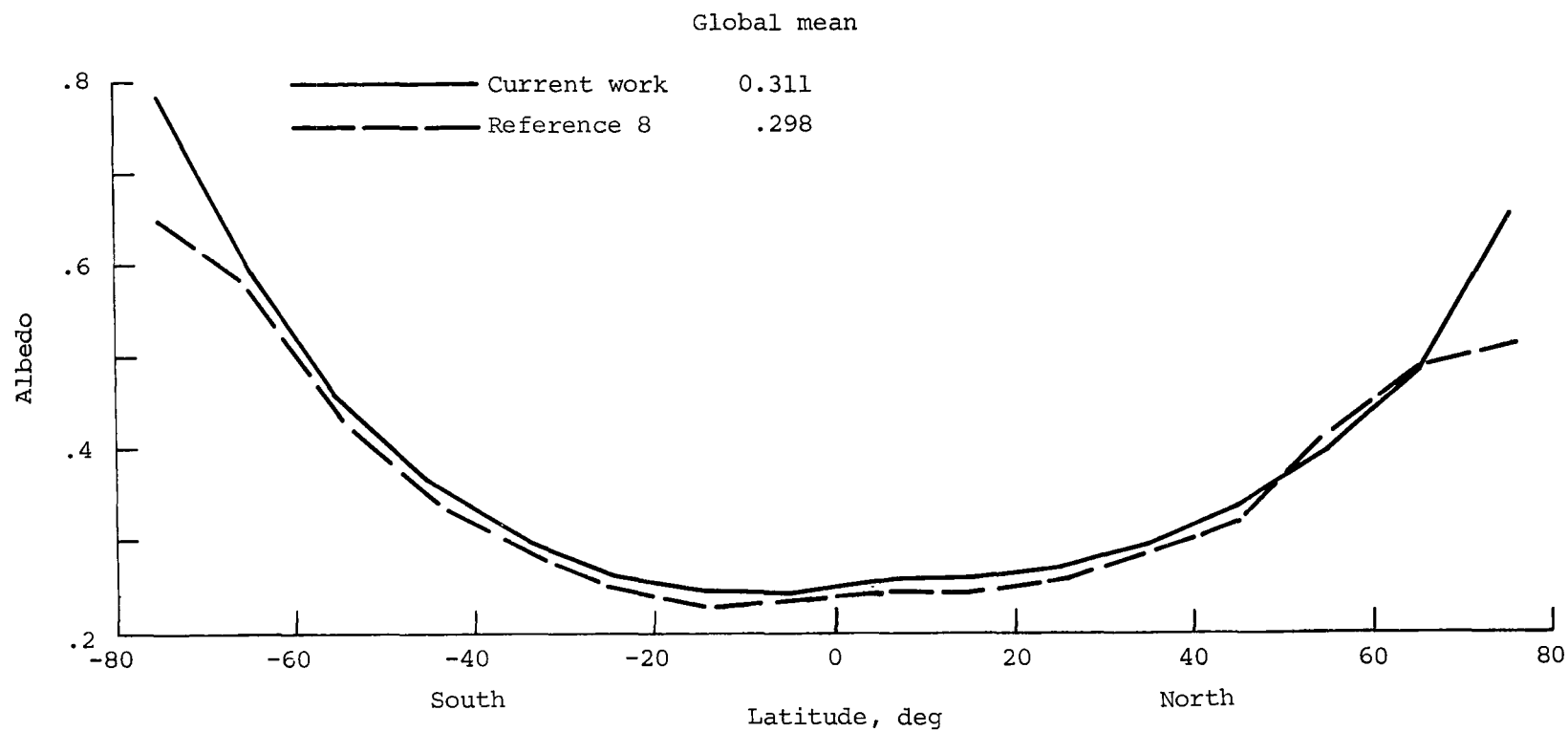
Reference 8   .298

(a) October.

Figure 10.- Comparison of albedo results with those of reference 8.
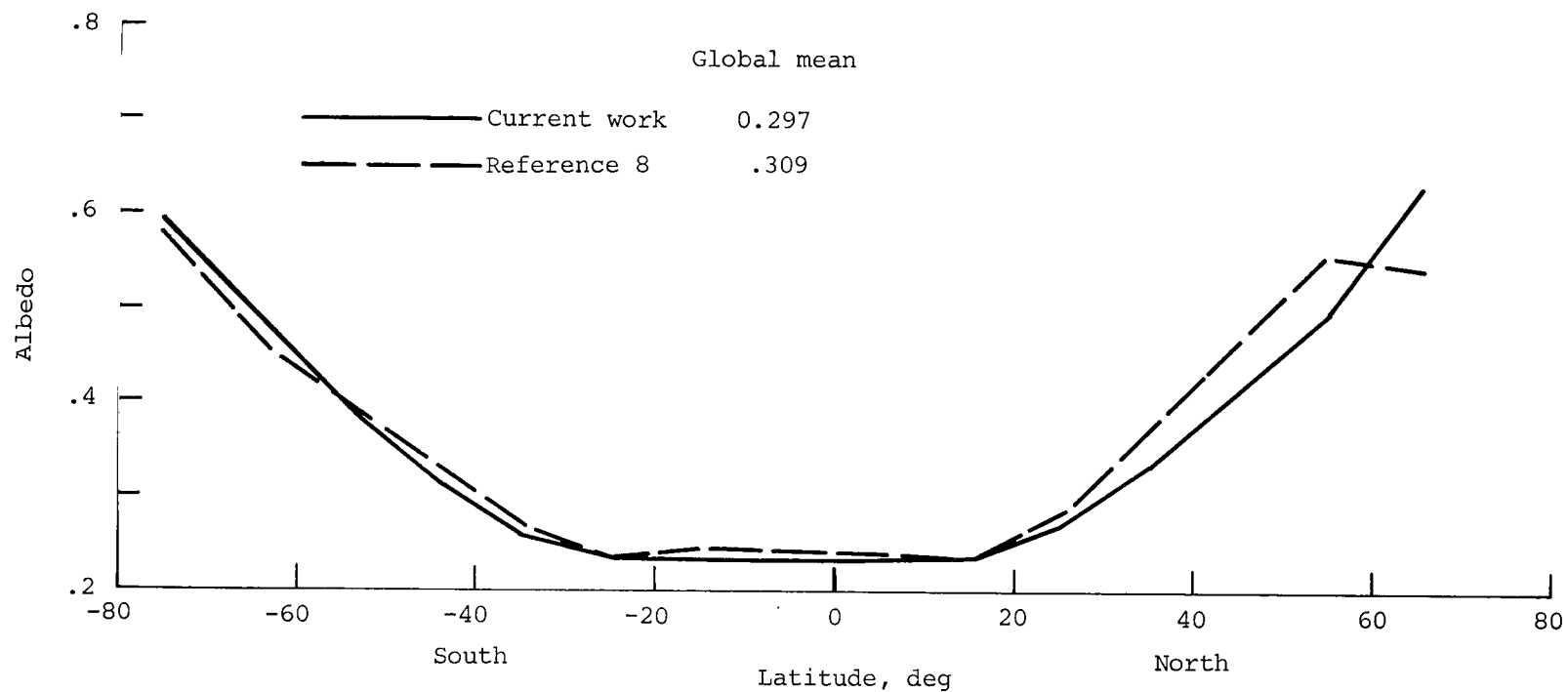
(b) January.

Figure 10.- Concluded.
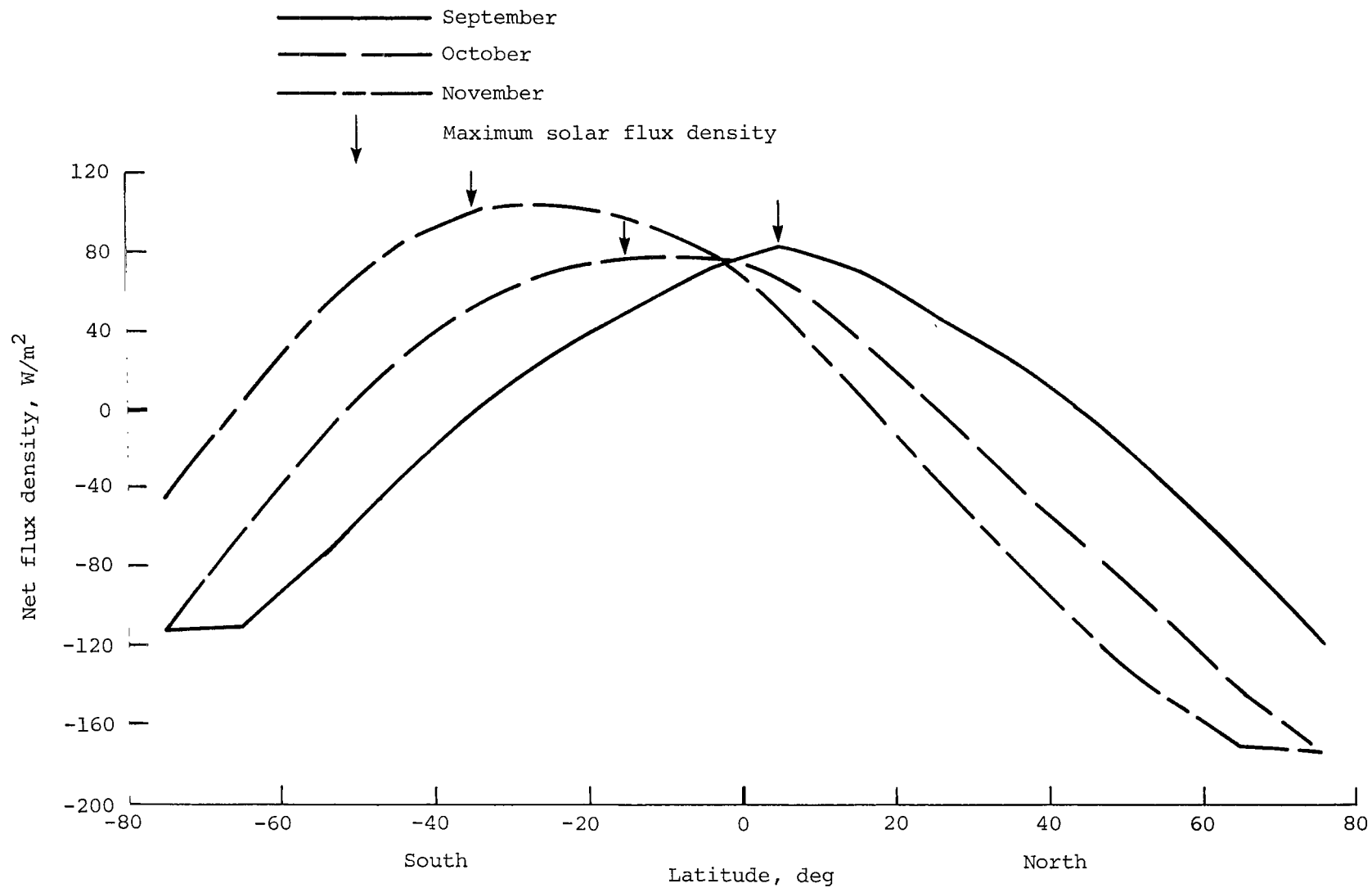
(a) September, October, November.

Figure 11.- Monthly averages of zonal net flux density for each month analyzed.
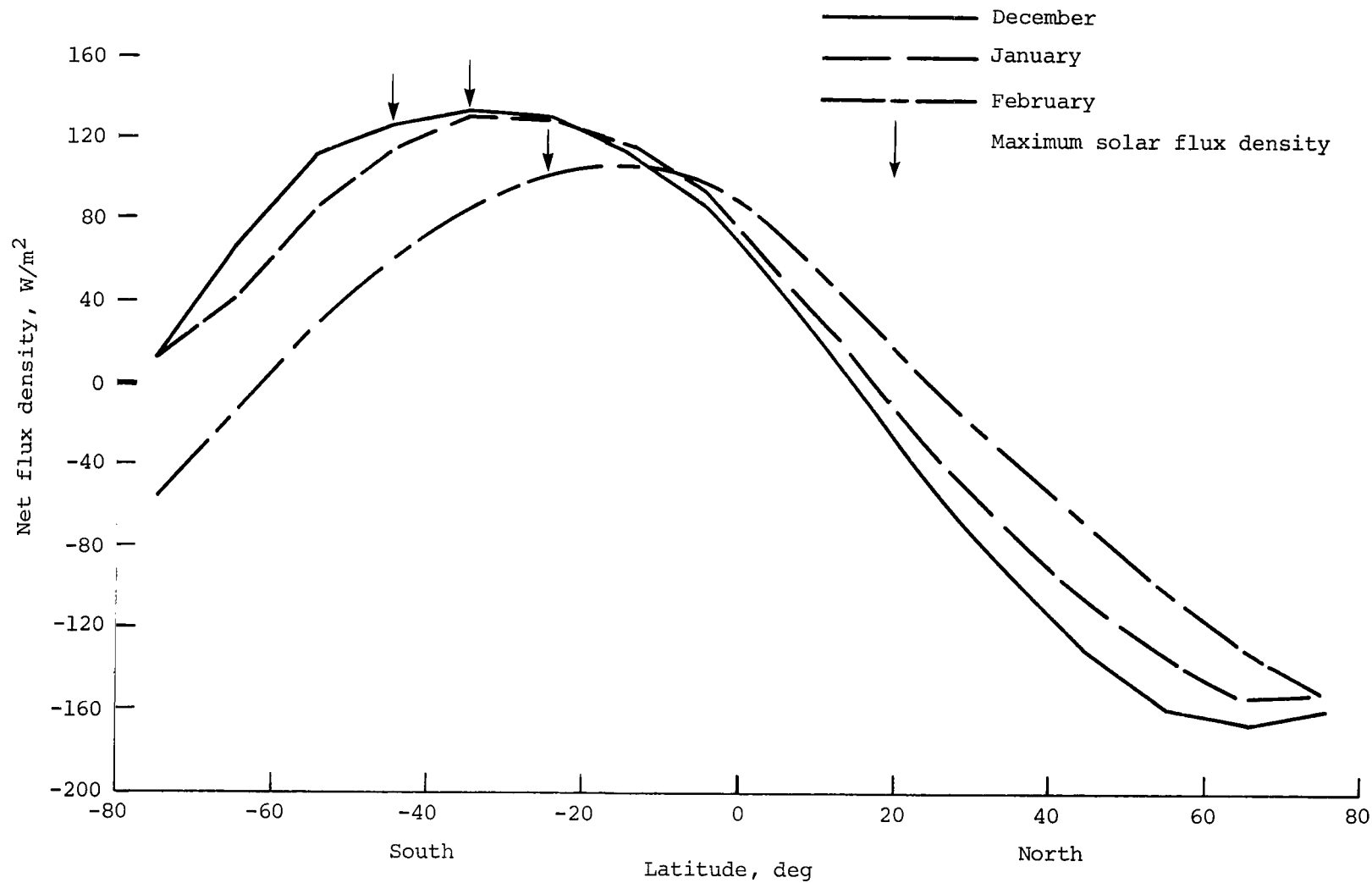
(b) December, January, February.

Figure 11.- Concluded.

Global mean, W/m^2

——————	Current work	4.0
— — — —	Reference 8	4.3
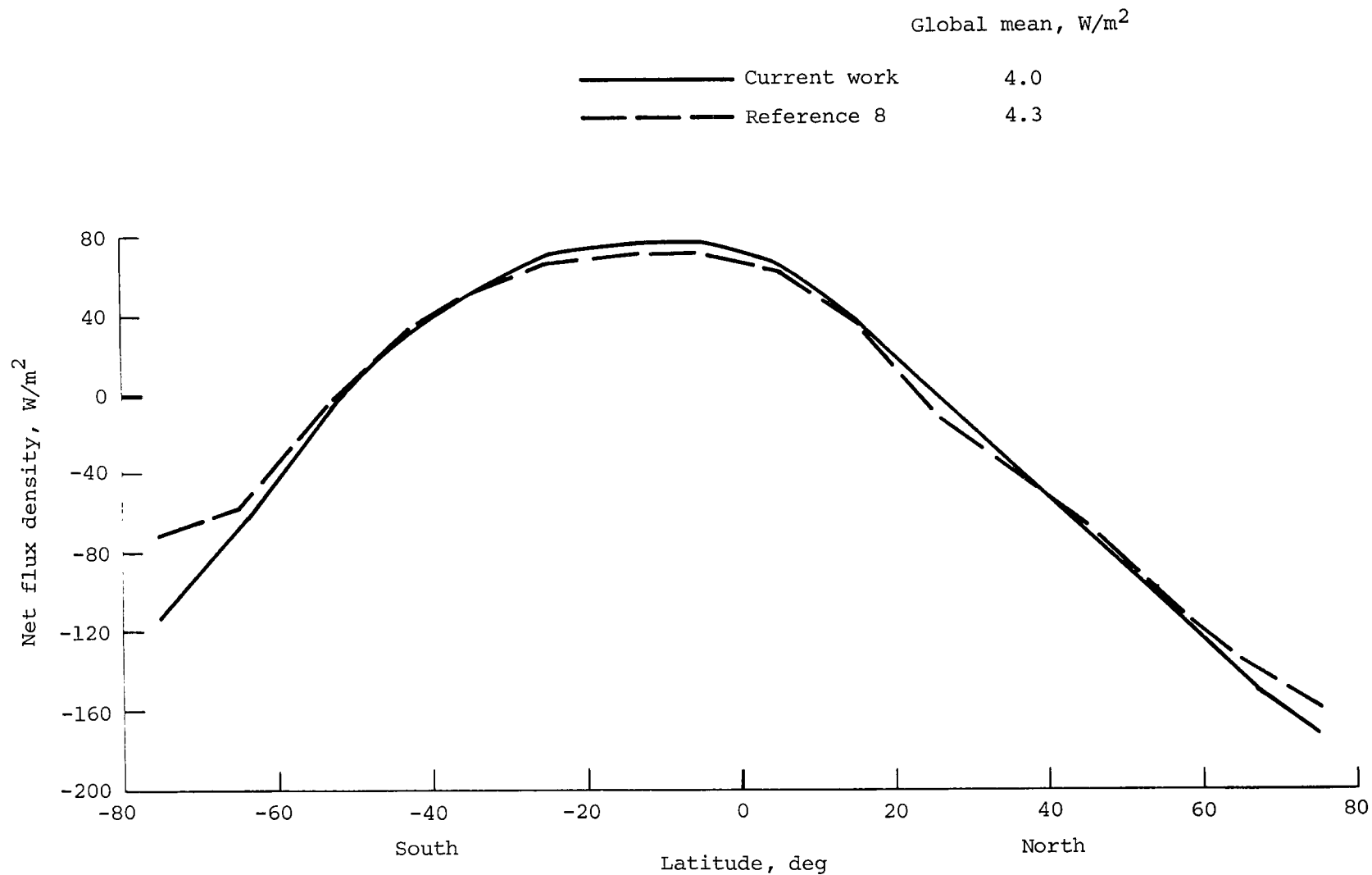
(a) October.

Figure 12.- Comparison of net flux density results with those of reference 8.
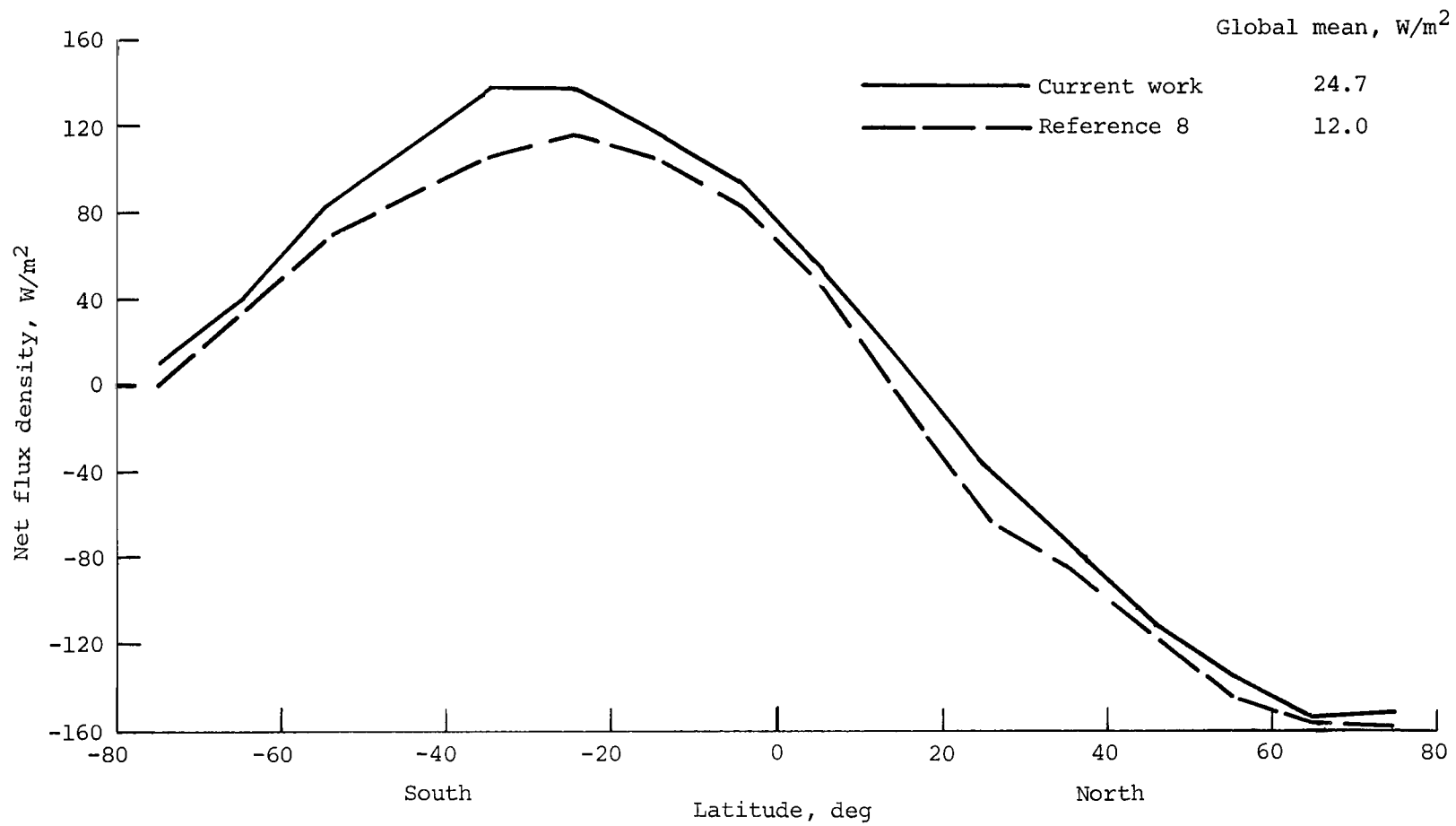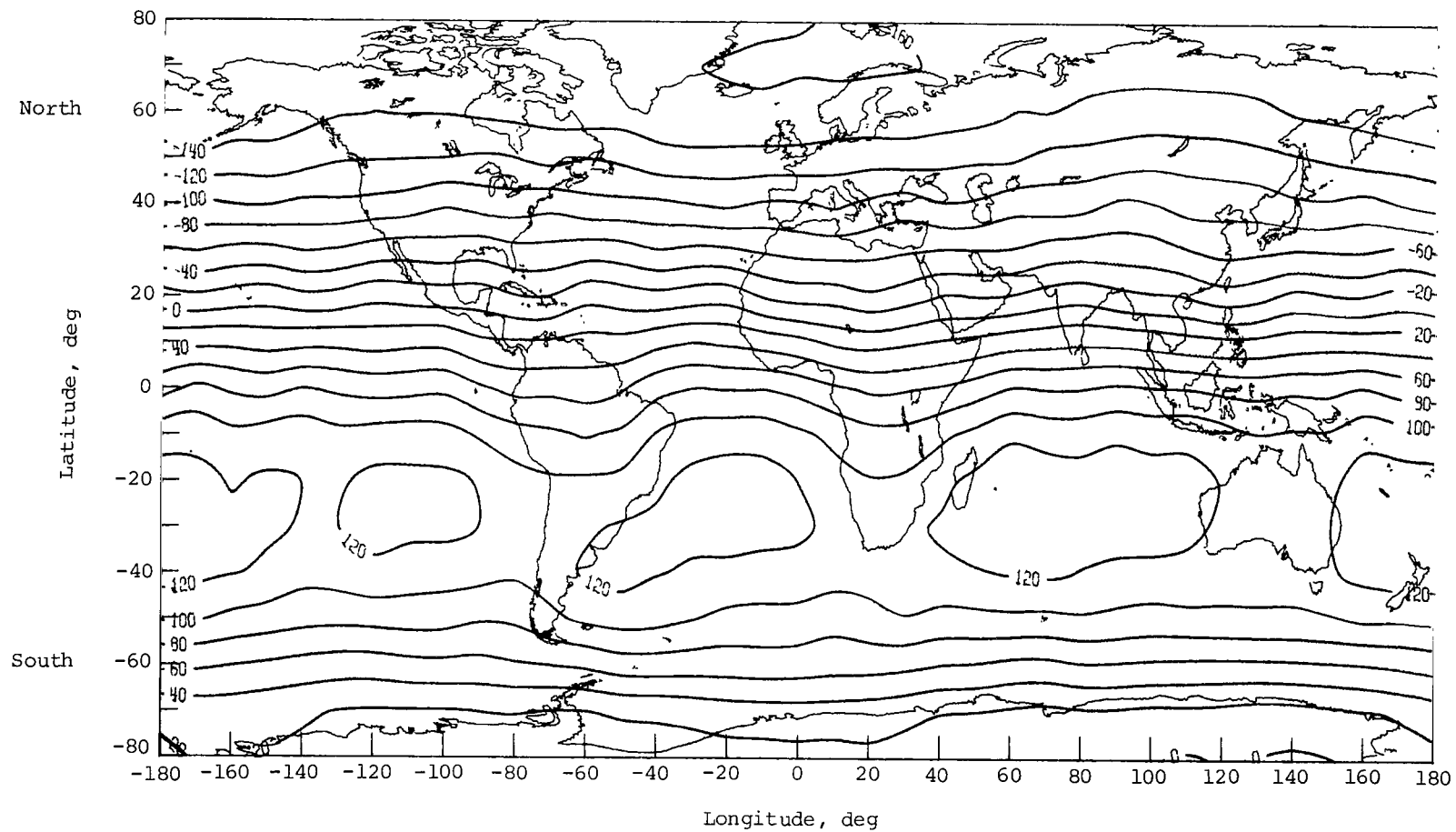
(b) January.

Figure 12.- Concluded.

Longitude, deg
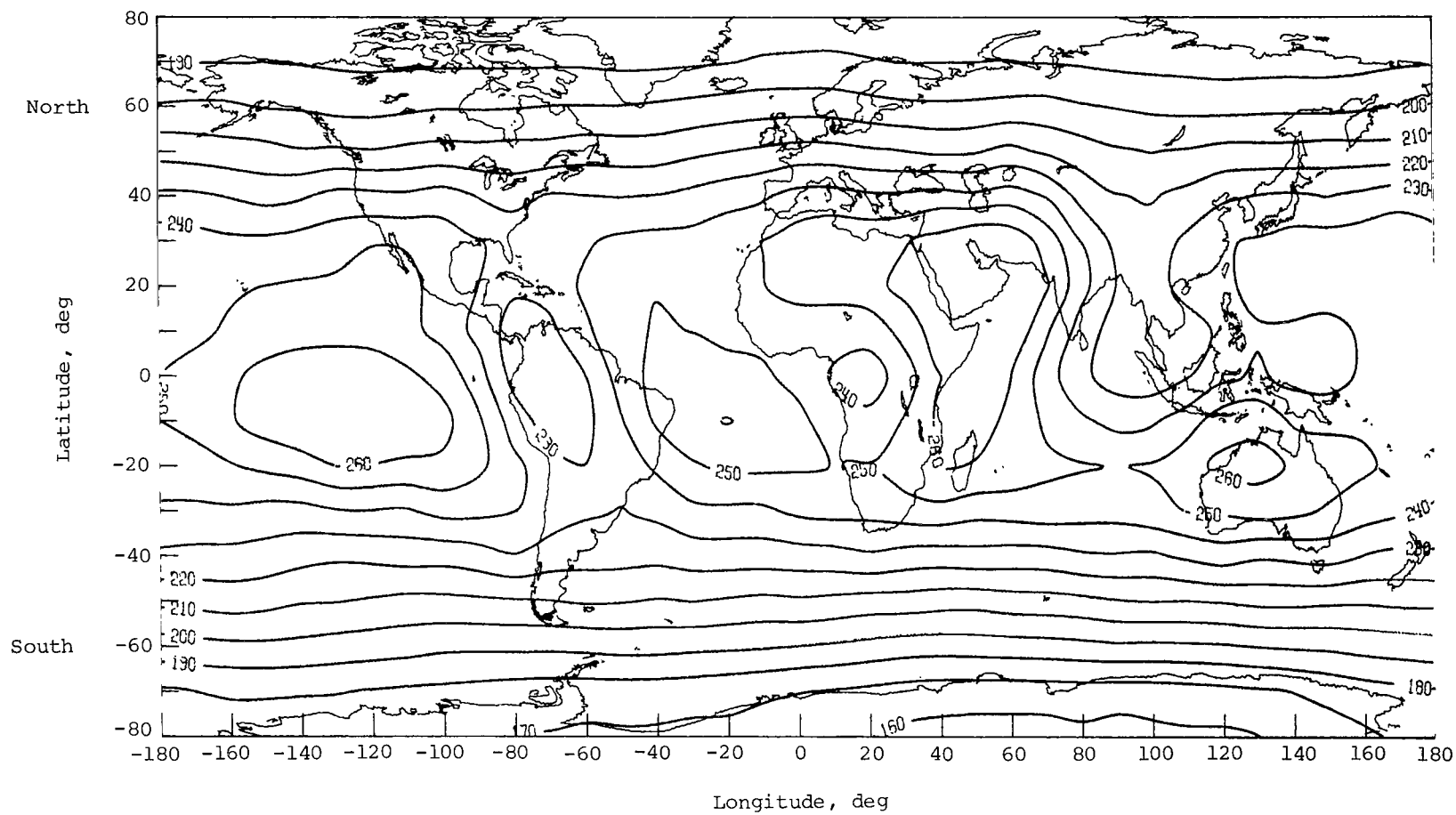
(a) October.

Figure 13.- Global distribution of emitted flux density for typical months (ESSA 7 data). Units are W/m^2.
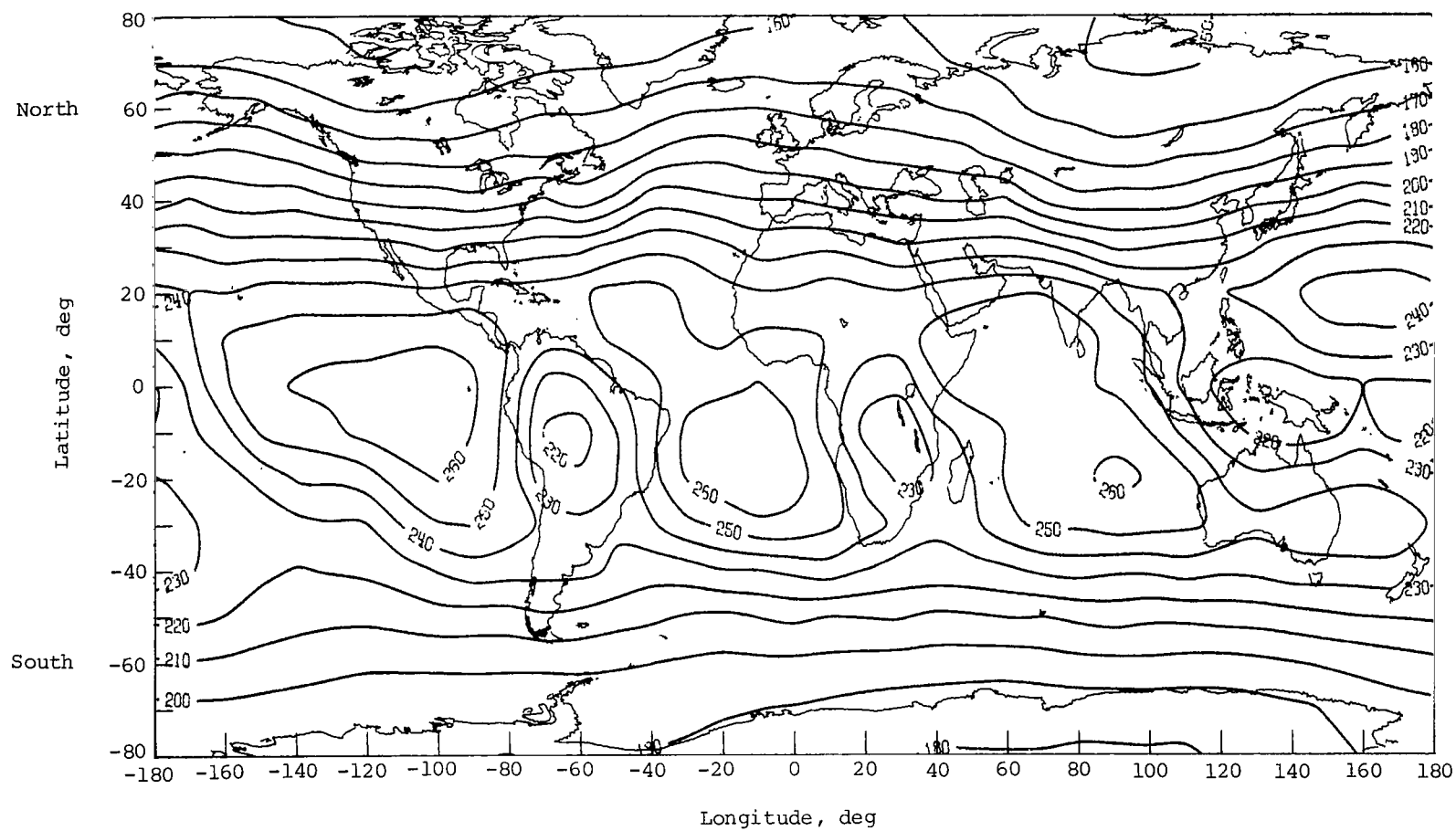
(b) January.

Figure 13.- Concluded.

Longitude, deg
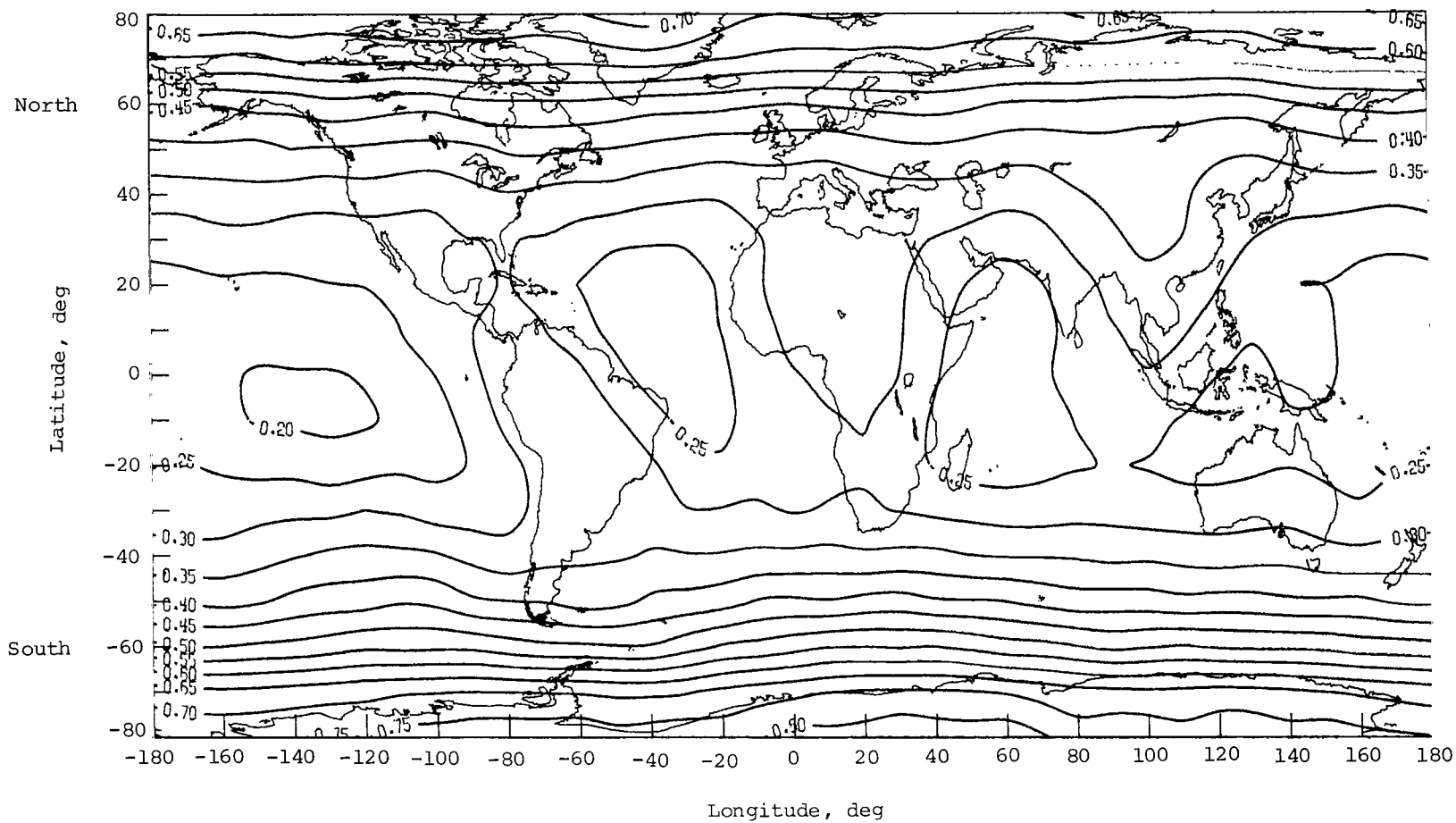
(a) October.

Figure 14.- Global distribution of albedo for typical months (ESSA 7 data).
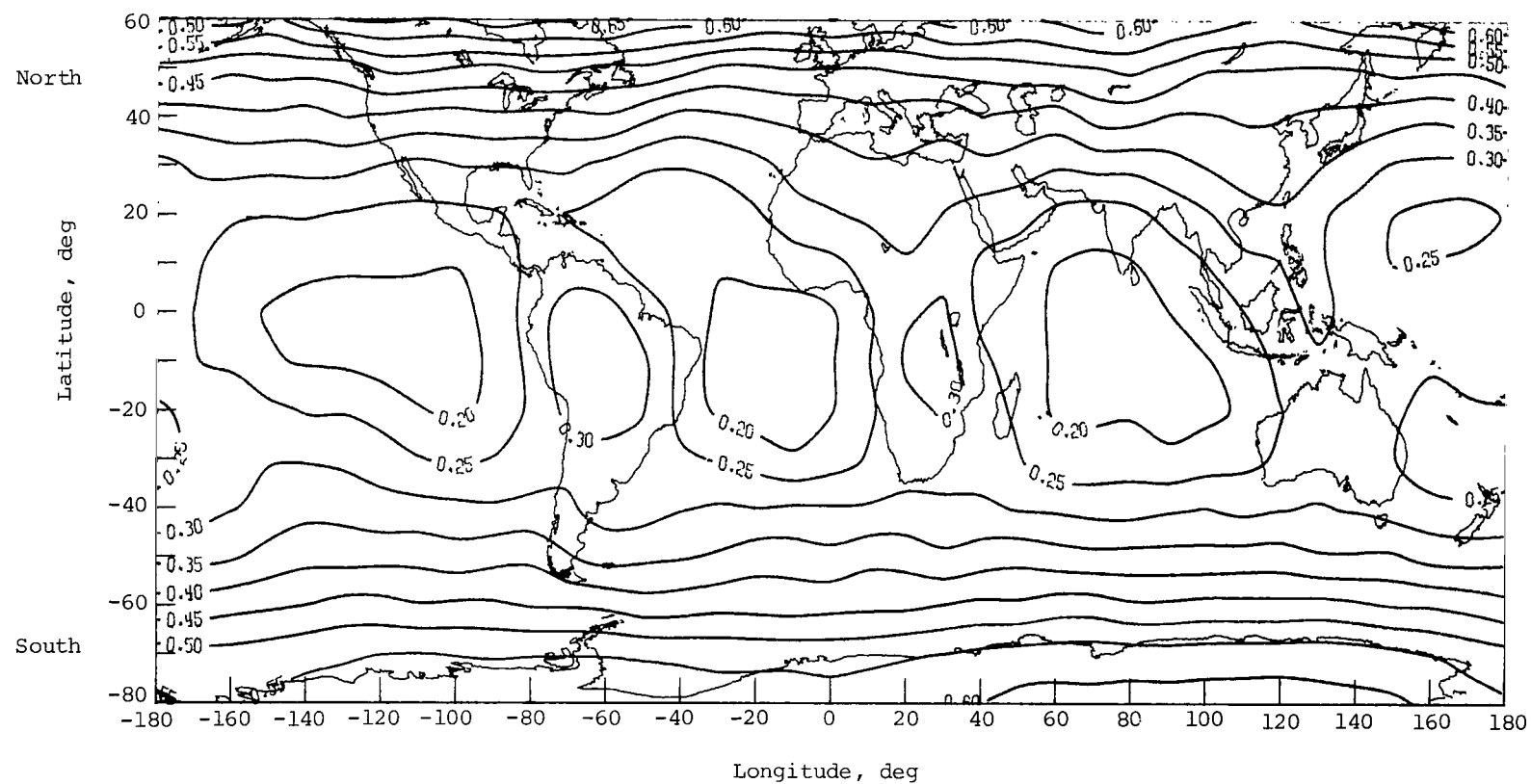
(b) January.

Figure 14.- Concluded.
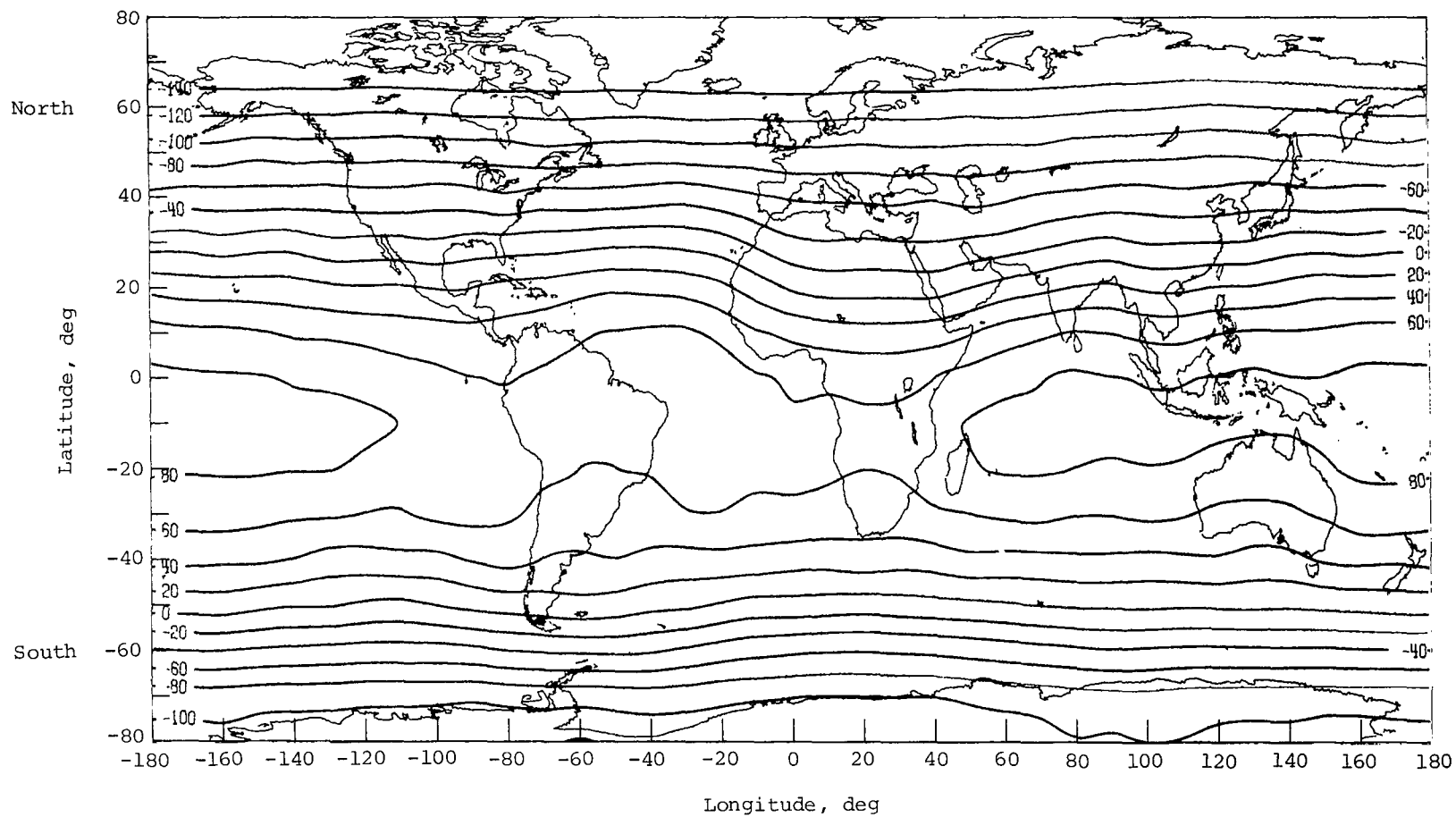
(a) October.

Figure 15.- Global distribution of net flux density for typical months (ESSA 7 data).
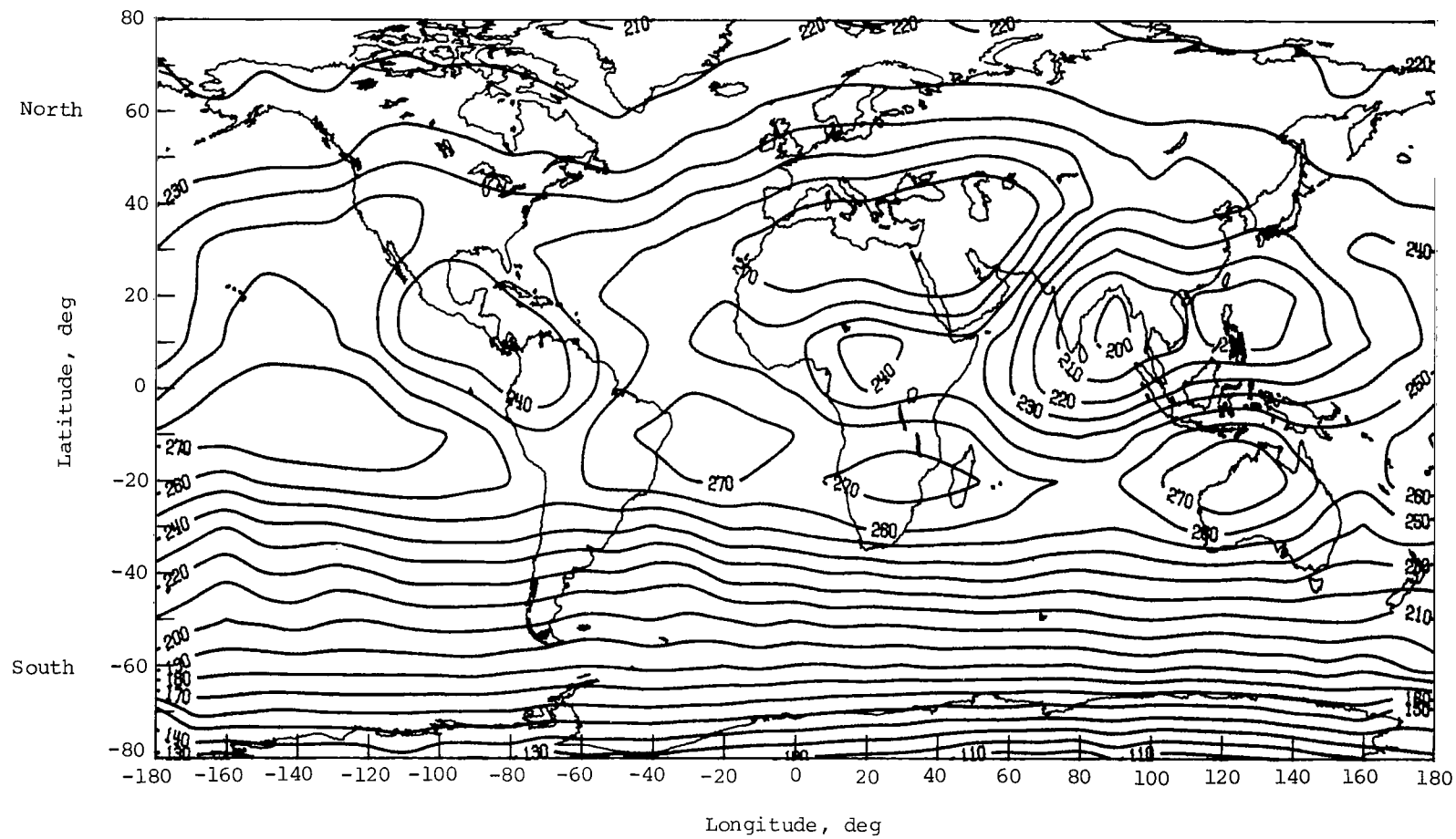Units are W/m^2.
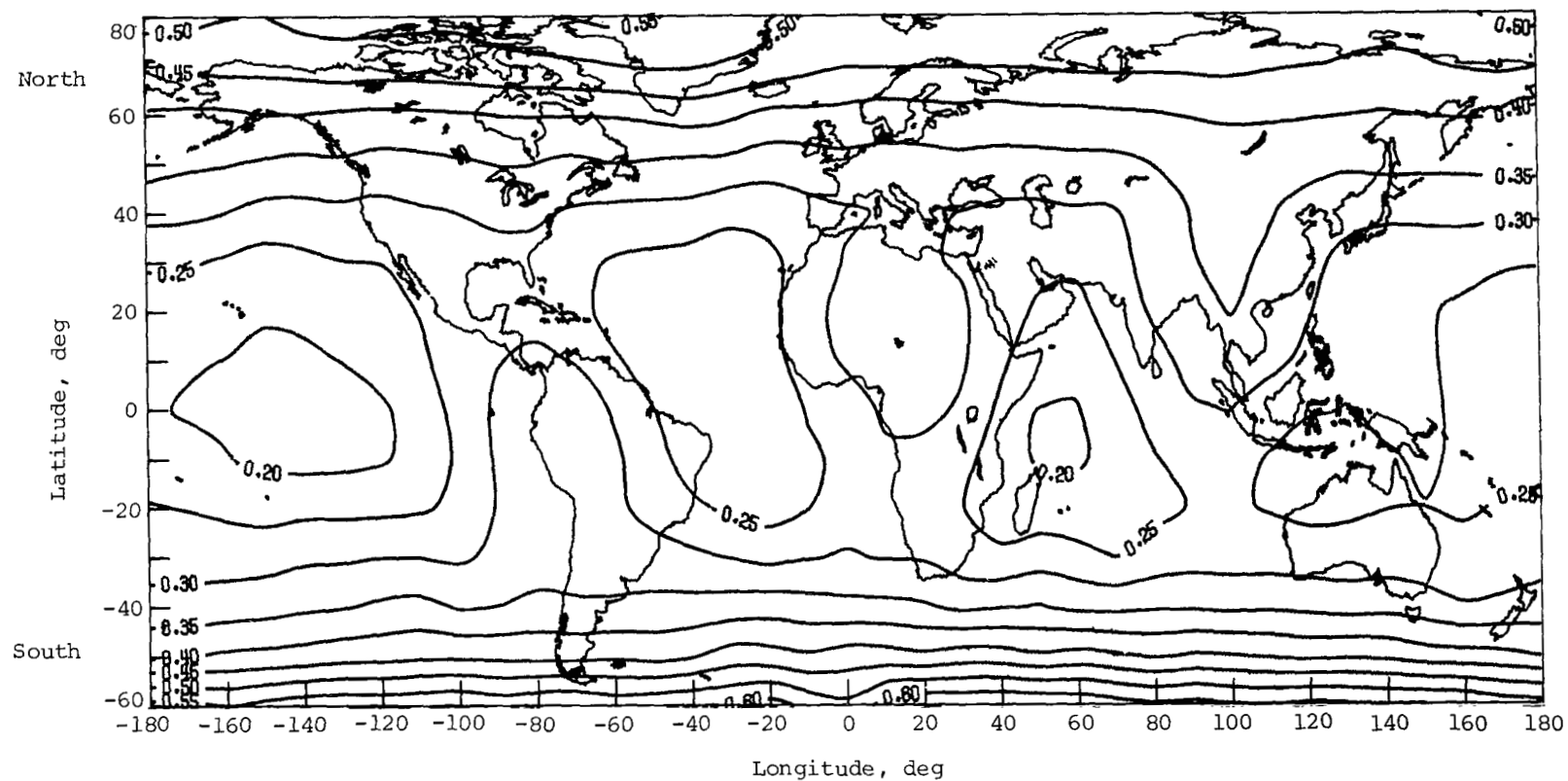
(b) January.

Figure 15.- Concluded.
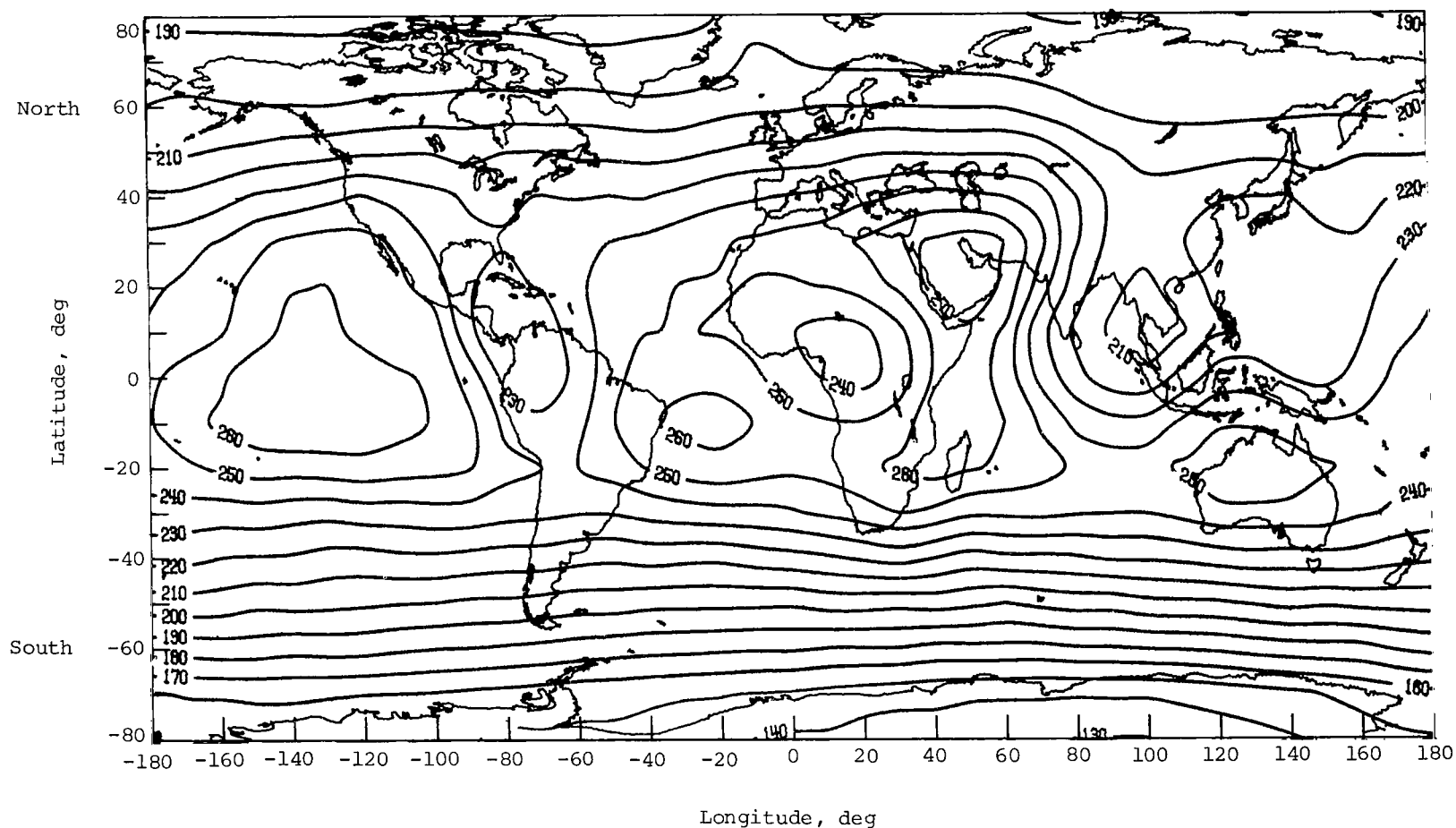
(a) ESSA 7, September 1968.

Figure 16.- Comparison of global distribution of emitted flux density between
results from ESSA 7 (Sept. 1968) and results from Nimbus 6 (Aug. 1975).
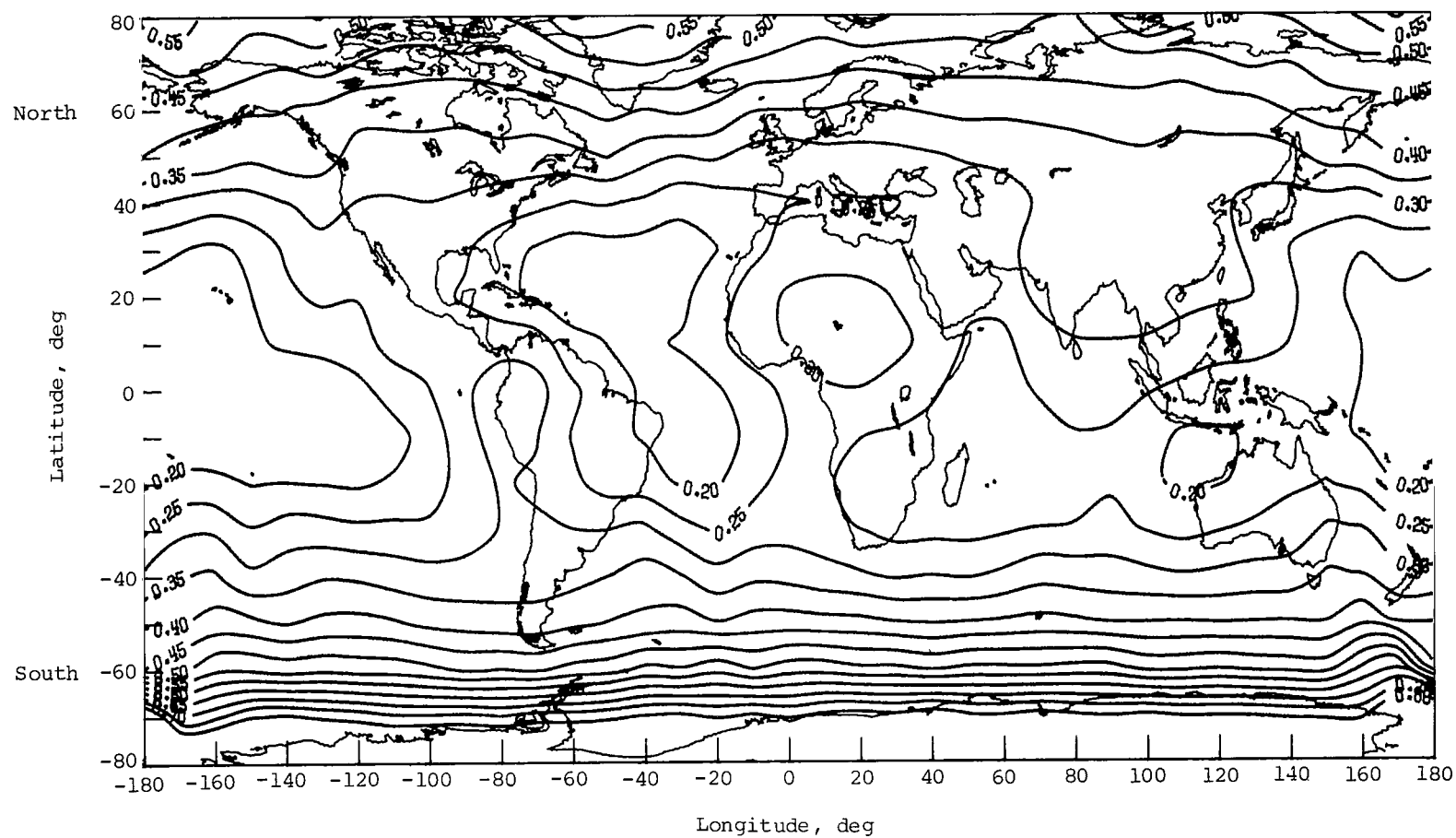Units are W/m^2.

(b) Nimbus 6, August 1975.

Figure 16.- Concluded.

(a) ESSA 7, September 1968.

Figure 17.- Comparison of global distribution of albedo between data from
ESSA 7 (Sept. 1968) and data from Nimbus 6 (Aug. 1975).
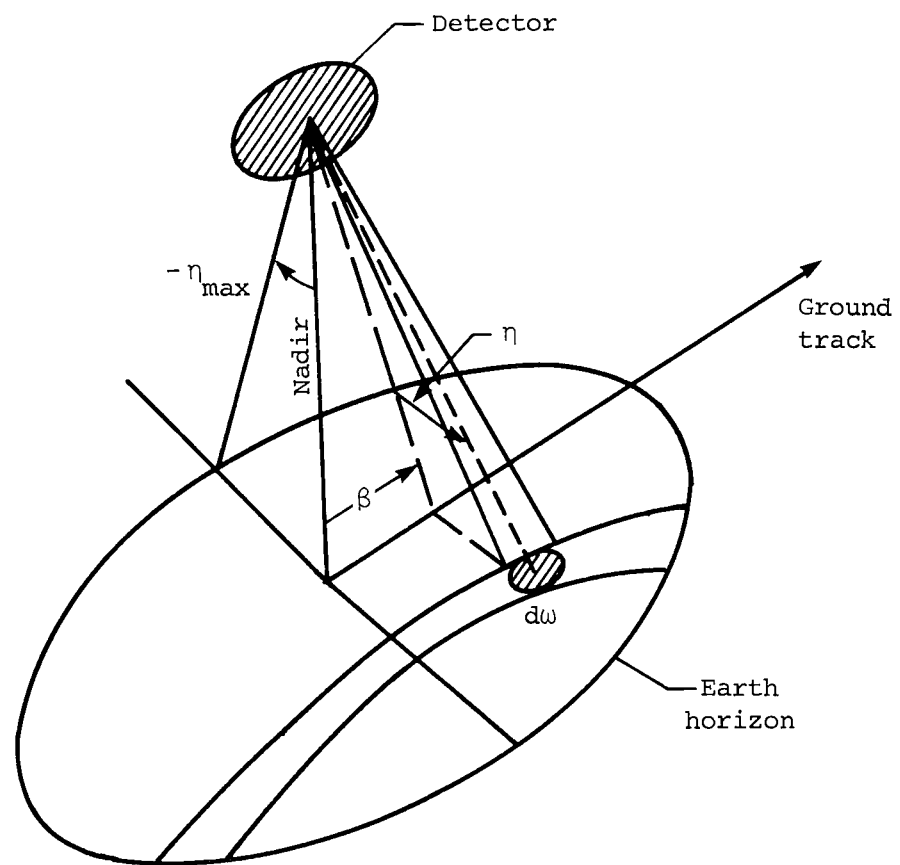
(b) Nimbus 6, August 1975.

Figure 17.- Concluded.

Figure 18.- Geometry for rotating flat-plate detector above Earth.

1. Report No.	2. Government Accession No.	3. Recipient's Catalog No.
NASA TP-1402		

4. Title and Subtitle	5. Report Date
ANALYSES OF EARTH RADIATION BUDGET DATA FROM UNRESTRICTED BROADBAND RADIOMETERS ON THE ESSA 7 SATELLITE	May 1979
	6. Performing Organization Code

7. Author(s)	8. Performing Organization Report No.
William L. Weaver and Frederick B. House	L-12587

9. Performing Organization Name and Address	10. Work Unit No.
	175-40-30-01
NASA Langley Research Center Hampton, VA 23665	11. Contract or Grant No.
	13. Type of Report and Period Covered

12. Sponsoring Agency Name and Address	Technical Paper
National Aeronautics and Space Administration Washington, DC 20546	14. Sponsoring Agency Code

15. Supplementary Notes

William L. Weaver: Langley Research Center, Hampton, Virginia.
Frederick B. House: Drexel University, Philadelphia, Pennsylvania.

16. Abstract

Six months of data (Sept. 1968 through Feb. 1969) from the wide-field-of-view low resolution infrared radiometers (LRIR) on the Environmental Science Services Administration (ESSA) 7 satellite were analyzed. Earth-emitted and Earth-reflected irradiances were computed at satellite altitude using data from a new in-flight calibration technique. Flux densities and albedos were computed for the top of the Earth's atmosphere (30 km). Monthly averages of these quantities over 10°-latitude zones, each hemisphere, and the globe are presented for each month analyzed, and global distributions are presented for typical months. Emitted flux densities are generally lower and albedos higher than those of previous studies. This may be due, in part, to the fact that the ESSA 7 satellite was in a 3-p.m. Sun-synchronous orbit and some of the comparison data were obtained from satellites in 12-noon Sun-synchronous orbits. ESSA 7 detectors seem to smooth out spatial flux density variations more than scanning radiometers or wide-field-of-view fixed-plate detectors. Significant longitudinal and latitudinal variations of emitted flux density and albedo were identified in the tropics in a zone extending about $\pm 25^{\circ}$ in latitude.

17. Key Words (Suggested by Author(s))	18. Distribution Statement
Earth radiation budget ESSA 7 Radiometer data Unrestricted field of view	Unclassified - Unlimited Subject Category 47

19. Security Classif. (of this report)	20. Security Classif. (of this page)	21. No. of Pages	22. Price*
Unclassified	Unclassified	54	$5.25

National Aeronautics and
Space Administration

Washington, D.C.
20546

Official Business
Penalty for Private Use, $300

THIRD-CLASS BULK RATE

U.S.MAIL

```
/    I  IU,E,        U43U79 SUU9U3DS
DEPT OF THE AIR FORCE
AF WEAPONS LABORATORY
ATTN: TECHNICAL LIBRARY (SUL)
KIRTLAND AFB NM 87117
```

POSTMASTER: If Undeliverable (Section 158
Postal Manual) Do Not Return